Contents lists available at ScienceDirect

Journal of the Mechanics and Physics of Solids

journal homepage: www.elsevier.com/locate/jmps

Frank-Read source operation in six body-centered cubic refractory metals

Shuozhi Xu[a,*], Yanqing Su[b], Lauren T. W. Smith[c], Irene J. Beyerlein[a,b,c]

[a] California NanoSystems Institute, University of California, Santa Barbara, Santa Barbara, CA 93106-6105, USA
[b] Department of Mechanical Engineering, University of California, Santa Barbara, Santa Barbara, CA 93106-5070, USA
[c] Materials Department, University of California, Santa Barbara, Santa Barbara, CA 93106-5050, USA

ARTICLE INFO

Article history:
Received 7 March 2020
Revised 13 April 2020
Accepted 29 April 2020
Available online 5 May 2020

Keywords:
Frank-Read source
Refractory metals
Phase-field dislocation dynamics
Density functional theory

ABSTRACT

The Frank-Read (FR) source is a well-known intragranular dislocation source that plays an important role in size-dependent dislocation multiplication in metallic crystals. In this work, we extend a phase-field dislocation dynamics (PFDD) technique to study FR source operation on the {110}, {112}, and {123} slip planes in body-centered cubic (BCC) crystals. Here, the periodic lattice potentials for shearing across these planes used in PFDD simulations are provided by density functional theory (DFT) calculations for six BCC refractory metals, Cr, Mo, Nb, Ta, V, and W. The DFT calculations show that the group 6 elements (Cr, Mo, and W) have higher generalized stacking fault energies than the group 5 elements (Nb, Ta, and V). With PFDD, we focus on the effects of the GSFE curve shape, initial character angle, slip plane crystallography, and elastic anisotropy (measured by the Zener ratio, A_c) on the critical stresses to activate the FR source. For the same FR source of any character angle in the same metal, the critical stress on the {123} plane is lower than those on the {110} and {112} planes. It is also shown that elastic anisotropy decreases the critical stress when $A_c < 1$ and increases it when $A_c > 1$. We also find that in both Cr and Nb, which possess the lowest values of A_c among the six metals, elastic anisotropy causes the critical stress on {110} planes to achieve a local maximum for the mixed 45° oriented FR source.

Contents

1. Introduction

During plastic deformation, dislocations multiply to increase their mobile density. Among all possible mechanisms of dislocation multiplication in a bulk single crystal in stage I work hardening (i.e., few interfering dislocations), the Frank-Read (FR) source (Frank and Read, 1950) is considered among the most prevalent. Particularly at relatively low strain rates, FR sources usually produce a larger amount of new dislocations than other sources such as homogeneous nucleation and nucleation from defects (e.g., grain boundaries, precipitates, voids) (Gurrutxaga-Lerma et al., 2015). At larger plastic strains, e.g., in stage II work hardening, dislocations on multiple slip systems intersect with each other, facilitating dislocation climb and cross-slip, reducing the mean free path of dislocations, and hence suppressing FR sources (Stricker et al., 2018).

The FR source is a straight dislocation segment pinned at two ends (Hull and Bacon, 2011). Under an applied stress, the segment bows out, extending its length and changing its configuration from straight to semi-elliptical, remaining pinned at its two ends during the process. At a critical applied stress, the configuration of the dislocation becomes unstable and it is no longer in equilibrium. The dislocation expands under no further increases in stress and folds back around the pinned ends, leaving the remaining parts of the moving dislocation as a loop that freely expands away from the source and recovering the initial segment of the source. Achieving the critical configuration entails glide of the dislocation line and creation of new dislocation line under tension. The critical stress is related to the lattice resistance to the motion of the dislocation and increase in energy as the dislocation lengthens (Anderson et al., 2017).

A number of computational models have been applied to study the dynamics of FR source operation. Atomistic simulations via molecular dynamics (MD) or molecular statics (MS) can simulate the FR source process, while naturally accounting for any dislocation core effects (de Koning et al., 2003; Li and Yang, 2006; Shimokawa and Kitada, 2014), yet the simulation cell sizes are usually limited to the submicron-scale (Xu and Chen, 2019); the time scales in MD simulations are usually exceptionally small (Chen et al., 2020). The phase-field crystal (PFC) model (Elder et al., 2002), which may be viewed as a simplified version of classical density functional theory (DFT), can describe complex defect evolution phenomena on atomistic length scales but advantageously over diffusive time scales, much longer than those in MD (Elder et al., 2007). Based on the atomic number density field, the free energy functional in PFC contains a two-point correlation function. Using a modified correlation function to account for dissociated dislocations in FCC crystals (Berry et al., 2012), Berry et al. (2014) simulated FR source operation, reporting a novel dipole-to-quadrupole FR source transformation when the applied strain rate was at five orders of magnitude lower than that of typical MD simulations.

A few multiscale atomic-continuum modeling approaches have been employed to study FR sources, namely the concurrent atomistic-continuum (CAC) method (Xu et al., 2015, 2018a, 2018b) and the coupled atomistic/discrete-dislocation (CADD) method (Anciaux et al., 2018; Cho et al., 2018; Hodapp et al., 2018). These models attempt to concurrently bridge the continuum and atomistic domains and when applied to FR source operation can simultaneously account for the effects of dislocation cores and long-range elastic stress fields. For face-centered cubic (FCC) metals, Xu et al. (2016) studied the effect of elastic anisotropy on the critical stress for an FR source, showing that while the analytical model agreed well with the simulation result for Al, the departure in critical stress was more significant for Cu and Ni, which both have a higher degree of elastic anisotropy. Further, by simulating much longer initial FR source lengths, $L_{FR} > 100$ nm, than possible with atomistic-only models, the CAC model showed that the ratio of the half-loop height to L_{FR} in the critical dislocation bow-out configuration decreases with increasing L_{FR}. Using CADD, Cho et al. (2018) studied the effects of solid solution hardening in alloys in FR source operation, finding that under the same applied shear stress, for the same initial FR source length, and within the same amount of time, the FR source emits fewer number of dislocations in Al-5%Mg than in pure Al.

Models that achieve even larger length and time scales are continuum-based models, such as discrete dislocation dynamics (DDD) (von Blanckenhagen et al., 2003; Shishvan et al., 2008) and the level-set method (Xiang et al., 2003). These approaches aim to simulate an ensemble of individual dislocations without resolving individual atoms. Huang et al. (2014) reported that the dislocation core size can strongly influence the critical activation stress and the critical dislocation bow-out configuration in an FR source. Fitzgerald (2010) and Fitzgerald et al. (2012) applied DDD to study screw and edge FR source operation in body centered cubic (BCC) Fe, which has an extremely high elastic anisotropy index, $A_c = 2C_{44}/(C_{11} - C_{12}) =$

* Corresponding author.
E-mail address: shuozhixu@ucsb.edu (S. Xu).

https://doi.org/10.1016/j.jmps.2020.104017

7.4436 at 912°C, where $A_c = 1$ corresponds to ideal elastic isotropy. It was shown that the critical stresses for both {110} and {112} slip planes in Fe were either higher or lower than those calculated using ideal elastic isotropy, depending on the initial character angle of the dislocation segment pinned at the FR source (Fitzgerald et al., 2012).

Another class of models that similarly aim to simulate the motion of many discrete dislocations are energy minimization based phase-field (PF) dislocation models (Rodney and Finel, 2001; Wang et al., 2001). Similar to the traditional PF method, the PF dislocation models assume that a free energy functional of order parameters can adequately describe the energetics of the system. The order parameters correspond to the regions in the crystal which may or may be slipped due to the passage of dislocation(s). When applied to FR source operation, PF dislocation models are capable of accounting for the effects of different energetic contributions, including the changes in elastic strain energy, the lattice potential associated with shearing the glide plane, and the work done by the externally applied stress. In earlier work in FCC metals, Wang et al. (2001) and Rodney et al. (2003) verified the PF dislocation model by showing that the critical stress to activate an FR source scales inversely with L_{FR}, in agreement with an analytical isotropic elasticity model. Later, Shen and Wang (2004) extended the PF dislocation model formulation to treat partial dislocations so that the dissociation dislocations in FCC crystals could be simulated. Since then the PF model for FCC dislocations have been adopted to study the formation of extended dislocations, stacking faults, and twins from grain boundaries (GBs) (Hunter and Beyerlein, 2015). However, PF dislocation models that can simulate dissociated dislocations have not been applied to study FR sources in FCC metals, to our best knowledge. Very recently, a few PF dislocation models were extended to BCC, e.g., the microscopic phase-field (MPF) model in studying the formation of equilibrium dislocation networks at GBs (Qiu et al., 2019), and the phase-field dislocation dynamics (PFDD) model in modelling shear loop expansion and double kink pair migration under stress (Peng et al., 2020). These PF dislocation studies focused on dislocations on the {110} slip plane. In BCC crystals, however, slip may take place on {110}, {112}, and {123} planes, and glide on all three slip planes plays an important role in the plasticity of BCC metals (Raabe, 1995; Terentyev et al., 2016).

In this study, we extend the PFDD technique to treat dislocation dynamics in all three slip families in BCC crystals. With this model, we study the influence of slip plane and elastic anisotropy on the operation of FR sources of pure screw, pure edge, and mixed characters. The critical stresses and corresponding threshold bow-out configuration to activate the sources are computed for three types of slip planes: {110}, {112}, and {123} in six BCC pure refractory metals (Cr, Mo, Nb, Ta, V, and W). Important properties for these metals needed in PFDD simulations, such as the periodic lattice potential to shear across a given crystallographic plane, are calculated from DFT. The results show that for FR sources of the same screw/edge character in the same metal, the critical stress for the {123} plane is lower than those for the {110} and {112} planes. We also find that elastic anisotropy decreases the critical stress when the index $A_c = 2C_{44}/(C_{11} - C_{12}) < 1$ and increases it when $A_c > 1$. In addition, in both Cr and Nb, which possess the lowest values of A_c among the six refractory metals, elastic anisotropy causes the 45° oriented FR source to attain a second maximum critical stress for the {110} plane.

The paper is structured as follows. First, in Section 2 and Section 3, respectively, the DFT calculation method is described and the results for the lattice potentials for the three glide planes {110}, {112}, and {123} in all six metals are discussed. We then follow with a brief presentation of the basic PFDD formulation before expanding on the extensions made to account for the lattice periodicity and slip systems for the three glide planes in Section 4.1–Section 4.4. Next, the model setup for the FR source is presented in Section 4.5. The appropriate simulation cell size is selected and the model is verified for a few simple cases against the analytical formula. Afterwards, we present results in Section 5 on the critical stress and bow-out configurations for activating FR sources, paying particular attention to the influence of GSFE curve shape, initial character angle, glide plane selection, and elastic anisotropy.

2. DFT Calculations

As will be fully described in Section 4.1, a number of important parameters are incorporated in the PFDD calculations, such as the lattice parameter a_0, elastic constants C_{11}, C_{12}, and C_{44}, and fault energies for specific crystallographic planes. The first four can be measured while the last one is usually provided by atomic-scale calculations (Su et al., 2019b). In this section, we use DFT to calculate a_0, C_{11}, C_{12}, C_{44}, and generalized stacking fault energy (GSFE) curve γ_{gsf} for the six BCC refractory metals that will be studied by PFDD. With DFT, we can compute material properties and defect energies for all six metals in a uniform way. With MS or MD, however, we would need to choose, for each metal, a different interatomic potential, which can have differing levels of accuracy (Xu et al., 2018c; 2017b). Further, for BCC pure metals, most interatomic potentials cannot reproduce well the GSFEs computed by DFT calculations (Chavoshi and Xu, 2019; Xu and Su, 2018) and for one of the metals we study, Cr, which is known to be antiferromagnetic, magnetism cannot be described by standard interatomic potentials.

DFT calculations are conducted using VASP (Kresse and Furthmüller, 1996). Based on the projector augmented wave method (Blöchl, 1994; Kresse and Joubert, 1999), a plane-wave basis with a cutoff energy of 600 eV is adopted. The number of valence electrons in pseudopotentials, N_{ve}, is summarized in Table 1. To approximate the exchange-correlation energy functional, the Perdew-Burke-Ernzerhof (PBE) formulation of the generalized gradient approximation (Perdew et al., 1996) is used. The conjugate gradient scheme is employed for the electronic self-consistent loop; the convergence is reached when the total free energy change between two steps are smaller than 10^{-4} eV (Su et al., 2020). The Brillouin zone is constructed by the Monkhorst-Pack scheme (Monkhorst and Pack, 1976), with a smearing width of 0.2 eV based on the Methfessel-

Table 1
A summary of the number of valence electrons per atom, N_{ve}, used in DFT calculations.

	Cr	Cr^{NM}	Mo	Nb	Ta	V	W
N_{ve}	12		12	11	11	13	12

Table 2
For each metal, three simulation cells are constructed in calculating γ_{gsf} with the y axis normal to the {110}, {112}, and {123} planes, respectively. In each simulation cell, presented are the number of unit cells, N_{uc}, the number of atoms, N_{at}, the number of atomic layers, N_{la}, and the number of atom layers near the top or bottom that are fixed during ionic relaxation, N_{tb}.

	{110}	{112}	{123}
N_{uc}	6	4	2
N_{at}	36	24	84
N_{la}	12	24	28
N_{tb}	2	3	4

Paxton smearing method (Methfessel and Paxton, 1989). Among the six metals, spin-polarization is considered only for Cr, wherein antiferromagnetism is assumed. Results using the nonmagnetic Cr calculations assumption are denoted as Cr^{NM}.

For a_0, C_{11}, C_{12}, and C_{44}, a periodic cell containing two atoms is used for each metal. The k-point mesh is $11 \times 11 \times 11$. For a_0, the simulation cell size is varied, with the free energy calculated for each size. a_0 corresponds to the cell size for the lowest bulk free energy. The cohesive energy E_{coh} is the energy of a free atom in a vacuum minus the lowest bulk free energy per atom. We note that the energy of a free atom in each metal is calculated in a cube of 15 Å $\times$ 15 Å $\times$ 15 Å with a single k-point, while magnetism is always assumed. With a_0 determined, C_{11}, C_{12}, and C_{44} are calculated via the energy-strain method provided in AELAS (Zhang and Zhang, 2017).

For γ_{gsf}, three slip planes {110}, {112}, and {123} are considered, via calculations in three different simulation cells for each metal. The crystallographic orientations of all simulation cells are designed such that the y axis is always along the slip plane normal and the z axis always points to the [111] direction. The numbers and positions of atoms in each unit cell and the crystallographic orientations are presented in Appendix A. In each simulation cell, along the y direction, N_{uc} unit cells are stacked one after another, before a 12 Å vacuum is added to one end. In this way, a series of non-interacting slabs, each of which has N_{at} atoms, are created.

In all γ_{gsf} calculations, $15 \times 1 \times 15$ k-points are adopted. Let the number of atomic layers along the y direction be N_{la}. The top $N_{la}/2$ layers of atoms are displaced by d_z with respect to the bottom $N_{la}/2$ atomic layers incrementally along the z[111] direction, until d_z reaches $b = \sqrt{3}a_0/2$, which is the magnitude of the Burgers vector of a perfect dislocation $\boldsymbol{b} = (a_0/2)\langle 111\rangle$. Following each displacement, the top N_{tb} and bottom N_{tb} layers of atoms along the y direction are fixed, while the remaining atoms in the middle are allowed to relax along the y direction. The ionic relaxation stops when the total energy between two steps is smaller than 10^{-3} eV/atom. In this way, each GSFE curve is represented by energies associated with 41 displacements. Values of N_{uc}, N_{at}, N_{la}, and N_{tb} in the three simulation cells are summarized in Table 2. Data for the GSFE curves in all six metals are available in Materials Cloud (Xu et al., 2020b).

3. DFT Results

3.1. Lattice parameter and elastic constants

Table 3 presents the lattice parameters, cohesive energies, and elastic constants calculated by DFT and compares them to the measured values reported by prior experimental studies (Kittel, 2004; Warlimont and Martienssen, 2018) for all six BCC refractory metals. Employing the commonly used index $A_c = 2C_{44}/(C_{11} - C_{12})$ as a measure of the degree of cubic elastic anisotropy, we find these metals span a relatively broad range of A_c. As known, W is elastically isotropic, with $A_c = 1$. The other metals are elastically anisotropic, wherein four of them have A_c lying below unity, e.g., Nb ($A_c = 0.5027$), and only one, Ta, has A_c above unity, i.e., $A_c = 1.5585$. Compared with Cr^{NM}, Cr has a larger a_0 and lower A_c. The finding that antiferromagnetism increases a_0 in Cr was also reported in a previous DFT work (Dezerald et al., 2014). More importantly, considering antiferromagnetism in Cr brings the predicted results of a_0 and ν^H closer to the experimental values. In Fe (Yan et al., 2004) and Ni (Su et al., 2019a), prior DFT calculations found that assuming ferromagnetism also increases a_0, which is in better agreement with experiments than when magnetism is not considered.

To isolate the effect of elastic anisotropy on FR source operation, we will repeat some PFDD calculations idealizing the material elasticity as isotropic. To this end, three ways have been used to define the two equivalent isotropic elastic constants, e.g., shear modulus μ and Poisson's ratio ν, from the three elastic constants, C_{11}, C_{12}, and C_{44}. These three,

Table 3
Lattice parameter a_0 (in Å), cohesive energy E_{coh} (in eV), elastic constants C_{11}, C_{12}, and C_{44} (in GPa), elastic anisotropy index A_c, isotropic shear modulus in Hill form μ^H (in GPa), and isotropic Poisson's ratio in Hill form ν^H, of the six BCC refractory metals. Results are based on this work (DFT) or prior experiments (Exp). All experimental results are from Warlimont and Martienssen (2018), except those of E_{coh}, which are from Kittel (2004).

	Method	Cr	Cr^{NM}	Mo	Nb	Ta	V	W
Group		6		6	5	5	5	6
a_0	DFT	2.864	2.846	3.160	3.324	3.320	2.999	3.184
	Exp	2.885		3.147	3.301	3.303	3.024	3.165
E_{coh}	DFT	4.1	4.1	6.35	6.91	8.33	5.39	10.41
	Exp	4.1		6.82	7.57	8.1	5.31	8.9
C_{11}	DFT	429.65	494.65	467.85	249.01	268.13	265.97	520.35
	Exp	348		465	245	264	230	523
C_{12}	DFT	59.94	142.37	158.75	135.43	160.35	139.84	199.88
	Exp	67		163	132	158	120	203
C_{44}	DFT	95.	99.05	100.22	18.1	77.38	26.24	142.42
	Exp	100		109	28.4	82.6	43.1	160
A_c	DFT	0.5139	0.5623	0.6485	0.3187	1.4359	0.4161	0.8888
	Exp	0.7117		0.7219	0.5027	1.5585	0.7836	1
μ^H	DFT	124.44	124.98	119.29	29.23	66.94	37.6	149.3
	Exp	114.62		124.22	37.55	69.14	47.52	160
ν^H	DFT	0.2232	0.2927	0.3022	0.4202	0.3469	0.4033	0.2906
	Exp	0.2118		0.2964	0.397	0.3402	0.3623	0.2796

Voigt (1889), Reuss (1929), and Hill (1952), are denoted by superscripts V, R, and H, respectively, and are expressed below,

$$\mu^V = \frac{C_{11} + 3C_{44} - C_{12}}{5} \tag{1}$$

$$\mu^R = \frac{5(C_{11} - C_{12})C_{44}}{3C_{11} - 3C_{12} + 4C_{44}} \tag{2}$$

$$\mu^H = \frac{\mu^V + \mu^R}{2} \tag{3}$$

and the Poisson's ratios as

$$\nu^V = \frac{C_{11} + 4C_{12} - 2C_{44}}{4C_{11} + 6C_{12} + 2C_{44}} \tag{4}$$

$$\nu^R = \frac{C_{11}^2 + 2C_{12}(3C_{44} - C_{12}) + C_{11}(C_{12} - 2C_{44})}{2[C_{11}^2 + C_{12}(C_{44} - 2C_{12}) + C_{11}(C_{12} + 3C_{44})]} \tag{5}$$

$$\nu^H = \frac{\nu^V + \nu^R}{2} \tag{6}$$

where the Hill averages μ and ν are simply the respective arithmetic means of the Voigt and Reuss averages.

In the isotropic PFDD calculations, we use the Hill average since it well reproduces the bulk modulus compared to measurements (Xu et al., 2019c). Table 3 lists the Hill average values. The DFT calculations show that group 6 elements (Cr, Mo, and W) have higher μ^H and lower ν^H than the group 5 elements (Nb, Ta, and V), a trend that is in agreement with experiments (Warlimont and Martienssen, 2018). Accounting for antiferromagnetism in Cr yields a similar μ^H but lower ν^H than without (Cr^{NM}), bringing the result in better agreement with experimental measurement.

3.2. Generalized stacking fault energies

Fig. 1 presents the GSFE curves for the six BCC refractory metals calculated using DFT for all three slip planes, {110}, {112}, and {123}. Each GSFE curve shows only one peak energy γ_{gsf}, which is termed the unstable stacking fault energy (USFE), γ_{usf}. The γ_{usf} for all six metals are summarized in Table 4, where we see that γ_{usf} for the group 6 elements (Cr, Mo, and W) are approximately twice as large as those for the group 5 elements (Nb, Ta, V). For the same metal, the {110} plane has the lowest γ_{usf} among the three slip planes. The highest γ_{usf} value lies on the {112} plane for the group 5 elements but on the {123} plane for the group 6 elements. We note, however, that the difference in γ_{usf} between the two higher order planes for the same metal is small, less than 3%. The ideal shear stress, τ_{is}, is the gradient of the GSFE curve, and the ideal shear strength, T_{is}, is the maximum value of τ_{is} (Kumar et al., 2020), i.e.,

$$\tau_{is}(d_z) = \frac{\partial \gamma_{gsf}(d_z)}{\partial d_z} \tag{7}$$

$$T_{is} = \max[\tau_{is}(d_z)] \tag{8}$$

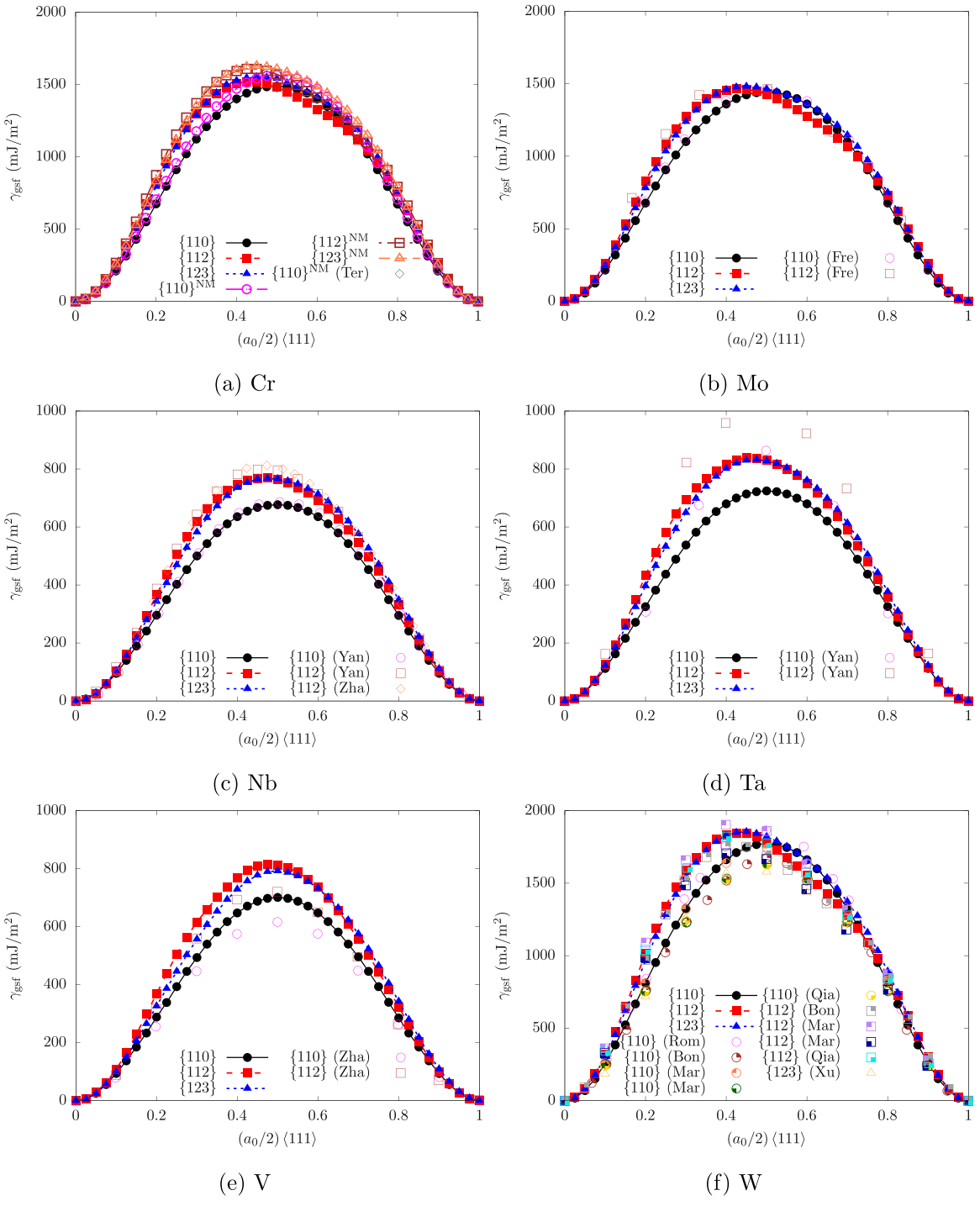

Fig. 1. Relaxed GSFE curves on three slip planes in six BCC refractory metals. Results are compared with those from previous DFT calculations, including Cr^{NM} (Terentyev et al., 2010), Mo (Frederiksen and Jacobsen, 2003), Nb (Yang and Qi, 2019; Zhang et al., 2011), Ta (Yang et al., 2001), V (Zhang et al., 2017), and W (Bonny et al., 2014; Marinica et al., 2013; Qian et al., 2018; Romaner et al., 2010; Xu et al., 2017a).

Values of T_{is} are also summarized in Table 4. These shear strengths constitute a theoretical shear limit and are far larger than the stresses required for dislocation glide or FR source activation. We find that following the γ_{usf} values, the group 6 metals have T_{is} values that are roughly twice as those of the group 5 metals.

Several studies have used DFT to calculate GSFE curves for various refractory metals and in Fig. 1, we compare the present results with GSFE curves in the literature. For most metals, the {110} and {112} GSFE curves are available, such as Mo (Frederiksen and Jacobsen, 2003), Nb (Yang and Qi, 2019; Zhang et al., 2011), Ta (Yang et al., 2001), V (Zhang et al.,

Table 4
USFEs, displacements for USFEs, and ideal shear strengths are denoted as γ_{usf} (in mJ/m^2), d_{usf} (in b), and T_{is} (in GPa), respectively. Different slip planes are distinguished by the superscripts 110, 112, and 123.

	Cr	Cr^{NM}	Mo	Nb	Ta	V	W
Group	6		6	5	5	5	6
γ_{usf}^{110}	1489.65	1564.98	1443.39	676.78	724.46	700.88	1772.74
T_{is}^{110}	19.79	20.76	17.7	7.51	7.78	8.27	20.99
γ_{usf}^{112}	1519.41	1608.34	1465.13	768.82	838.39	815.81	1845.83
d_{usf}^{112}	0.425	0.450	0.425	0.475	0.450	0.475	0.425
T_{is}^{112}	24.37	26.11	21.67	9.88	11.4	10.75	26.46
γ_{usf}^{123}	1552.05	1628.15	1481.35	767.42	832.34	792.14	1854.3
d_{usf}^{123}	0.450	0.450	0.450	0.475	0.475	0.500	0.450
T_{is}^{123}	23.42	24.65	20.35	8.91	9.97	9.66	24.99

2017), and W (Bonny et al., 2014; Marinica et al., 2013; Qian et al., 2018; Romaner et al., 2010; Xu et al., 2017a). Only for W has the {123} GSFE curve also been calculated by DFT (Xu et al., 2017a). For Cr, we can only compare our Cr^{NM} GSFE curve with prior DFT studies since magnetism was not taken into account previously (Terentyev et al., 2010). For the most part, the present results agree quantitatively with previous DFT results, with the exception of Ta and V, wherein our results provide lower and higher γ_{gsf}, respectively. For Ta, Yang et al. (2001) employed the full-potential linear muffin-tin orbital method, instead of the PBE formulation used in this work. For V, Zhang et al. (2017) used six {110} and ten {112} atomic planes, respectively, while we use 12 {110} and 24 {112} atomic planes. DFT calculations in FCC metals have shown that the GSFE values predicted by a simulation cell with six {111} atomic planes can differ from one with 12 {111} planes by more than 100 mJ/m^2 (Su et al., 2019a).

For Cr, magnetism is found to have an effect; Cr predicts lower γ_{gsf} and a lower T_{is} than Cr^{NM}. In previous DFT calculations, ferromagnetic Ni (Brandl et al., 2007; Su et al., 2019a) predicts higher γ_{gsf} values than nonmagnetic Ni, while nonmagnetic Fe (Yan et al., 2004) gives unphysical, negative γ_{gsf} curves. Here we find that the unrealistic case Cr^{NM} is not associated with negative γ_{gsf}. Still, in PFDD simulations that follow, we consider only the results for the realistic Cr accounting for antiferromagnetism.

Another quantity of interest in the GSFE curves is the displacement for γ_{usf} which is denoted as d_{usf} (see Table 4). According to the hard-sphere model, d_{usf} for the {110}, {112}, and {123} planes, are $b/2$, $b/3$, and $b/3$, respectively, suggesting that the {110} GSFE curves would be symmetric with respect to $b/2$ but the {112} and {123} curves would not. From the DFT calculations we see that indeed the {110} GSFE curves are symmetric and the {112} and {123} GSFE curves are not (except the {123} curve in V). However, for the latter two planes, the d_{usf} values are not $b/3$, but much larger and material dependent, ranging from $0.425b$ to $0.5b$.

4. PFDD Simulations

4.1. Present PFDD model formulation

Here, without loss of generality, we focus the PFDD description to dislocations moving within a single slip plane in a BCC crystal. An order parameter ϕ is introduced for the states of slip along a $<111>$ direction, wherein values $\phi = 0$ and 1 represent the unslipped and slipped states, respectively.

Let $\boldsymbol{u}$ represent the displacement field, $\boldsymbol{\beta} = \nabla \boldsymbol{u}$ the distortion field, and $\boldsymbol{\epsilon} = \mathrm{sym}\,\boldsymbol{\beta}$ the strain field. The total energy density ψ is the sum of the elastic energy density ψ_{ela}, the GSFE density ψ_{gsf}, and the external energy density ψ_{ext}, i.e.,

$$\psi(\boldsymbol{\epsilon}, \phi) = \psi_{ela}(\boldsymbol{\epsilon}, \phi) + \psi_{gsf}(\phi) - \psi_{ext}(\phi) \tag{9}$$

where

$$\psi_{ela}(\boldsymbol{\epsilon}, \phi) = \frac{1}{2}[\boldsymbol{\epsilon} - \boldsymbol{\epsilon}^p(\phi)] \cdot \boldsymbol{C}[\boldsymbol{\epsilon} - \boldsymbol{\epsilon}^p(\phi)] \tag{10}$$

$$\psi_{gsf}(\phi) = \frac{\gamma_{gsf}(\phi)}{l_{gsf}} \tag{11}$$

$$\psi_{ext}(\phi) = \boldsymbol{\sigma}_{app} \cdot \boldsymbol{\epsilon}^p(\phi) \tag{12}$$

where $\boldsymbol{C}$ is the elastic tensor, $\boldsymbol{\epsilon}^p = \mathrm{sym}\,\boldsymbol{\beta}^p$ is the plastic strain, γ_{gsf} is the GSFE per unit area, l_{gsf} is the interplanar spacing between two adjacent slip planes based on which γ_{gsf} is calculated, $\boldsymbol{\sigma}_{app}$ is the applied stress tensor, and the plastic distortion is given by

$$\boldsymbol{\beta}^p(\phi) = \frac{b\phi}{d_{sp}} \boldsymbol{s} \otimes \boldsymbol{n} \tag{13}$$

where $\boldsymbol{s}$ is the slip direction, $\boldsymbol{b} = b\boldsymbol{s}$, $\boldsymbol{n}$ is the slip plane unit normal, and d_{sp} is the interplanar spacing between two adjacent slip planes. Here, $d_{sp} = l_{gsf}$, and slip is confined to the preset habit planes (Xu et al., 2020a).

The time-dependent Ginzburg-Landau (TDGL) equation is employed to recursively minimize the total energy with respect to ϕ, i.e.,

$$\dot{\phi} = -m_0 \partial_\phi (\psi_{\text{ela}} + \psi_{\text{gsf}} - \psi_{\text{ext}}) \tag{14}$$

where the superposed dot denotes the time derivative and the Ginzburg-Landau coefficient m_0 is non-negative and constant. To highlight the dislocations, the continuum disregistry field ξ is calculated as an instantiation of the discrete atomic displacements (Xu et al., 2019a), i.e.,

$$\xi = \phi \boldsymbol{b} \cdot \boldsymbol{s} = \phi b \tag{15}$$

4.2. Comparison with other PF dislocation models for BCC systems

As mentioned in Section 1, there are currently two PF dislocation models for BCC systems in the literature: the MPF model (Qiu et al., 2019) and a recently developed PFDD model for BCC systems (Peng et al., 2020), which we denote as PFDD† for clarity. The present model adopts the same basic formulation as used in these two models Eq. (9)–(14), and the differences result from a few optional modeling choices. For γ_{gsf}, the MPF model uses a 2D GSFE surface and two order parameters per {110} slip plane, for each of which the slip direction is along a $<111>$ direction, whereas in the present model we use a 1D GSFE curve and only one order parameter. Employing two $<111>$ slip directions is possible for the {110} slip plane, but not generally for the {112} or {123} planes since there is only one $<111>$ direction in each higher order plane. In PFDD†, a 1D GSFE curve is used and the GSFE density contains a dislocation line orientation dependence and is expressed as

$$\psi_{\text{gsf}}(\phi) = \frac{\gamma_{\text{usf}} \Lambda(\theta) \sin^2(\pi\phi)}{l_{\text{gsf}}} \tag{16}$$

where γ_{usf} is used to account for the energy barrier against dislocation glide, θ is the local character angle, the angle subtended between the line orientation and the Burgers vector, and $\Lambda(\theta)$ is the function to account for the screw/edge character-dependent energy barrier. The $\Lambda(\theta)$ function can be informed by atomistic calculations and in the application of PFDD†, Peng et al. (2020) developed $\Lambda(\theta)$ based on Peierls stress calculations by MS simulations on the {110} planes in Ta by Kang et al. (2012). For the calculations in the current paper, the function $\Lambda(\theta)$ is not employed since the forms of $\Lambda(\theta)$ for other BCC metals (i.e., other than Ta) on the {110} plane and for any BCC metal on the non-{110} planes are generally unknown and it is desirable to treat dislocation dynamics on all three types of slip planes in a consistent manner.

4.3. Comparison with DDD and atomistic modeling

In DDD, dislocations are treated as discrete lines which, in the numerical implementation, are a set of segments connected by nodes (Zbib et al., 1998). The forces on the segments or nodes are calculated based on the elastic interactions between segments and the externally applied stress. These two terms are analogous to the elastic energy density Eq. (10) and external energy density Eq. (12) in PFDD. The forces then drive the dislocation dynamics on pre-set crystallographic glide planes, but without considering the inter-slip-planar spacings. As a dynamics approach, the strain rate takes effect (Gurrutxaga-Lerma et al., 2015). Some extended DDD codes incorporate information from atomistic simulations in order to represent the broad dislocation core sizes characteristic of dislocations in FCC crystals (Martínez et al., 2008). In simulating FR source operation, most DDD simulations consider the increase in elastic energy as the dislocation bows out and the changes in the elastic interactions between all dislocation segments. However, like the line tension model, the lattice energy to shear the planes is not considered in DDD simulations.

PFDD differs from DDD in four main ways. First, the lattice energy is directly taken into account as the GSFE density (Eq. (11)). Because of this, the formulation is able to consider, for instance, the effect of magnetism on the GSFE of Cr on dislocation motion. Second, the TDGL Eq. (14) results in energy minimized dislocation statics for a given applied stress. Unlike DDD, the "time" in PFDD is not physical time, but a unitless parameter. This is analogous to the damped dynamics method used in MD and dynamic CAC (Xu et al., 2017c). Third, the inter-slip-planar distance is not considered in DDD while it is in PFDD by using grid spacings with atomic resolution in the latter. Last, the dislocation lines are not explicitly tracked in PFDD, but formed naturally as the boundaries between slipped and unslipped regions.

Compared with atomistic modeling in which BCC lattices are used, PFDD employs a rectangular grid. Recent simulations based on the discrete Peierls-Nabarro model, which is similar to PFDD, showed that adopting a rhombic grid brought the Peierls stress closer to the experimental values by 20%–30% (Edagawa et al., 2019). In the current PFDD application, the GSFE curve does not vary with the applied stress. On the other hand, an MS simulation in BCC Fe found that the core structure of an edge dislocation on a {112} plane changes subject to an applied stress (Monnet and Terentyev, 2009).

4.4. Method extension to higher order planes in BCC systems

To solve the continuum PFDD model, a 3D grid is used for numerical discretization. By systematically studying the effects of grid spacings in PFDD simulations on the predicted disregistry in FCC metals, Xu et al. (2020a, 2019b) showed that, for

Table 5
For an FR source with a given character angle, three simulation cells are constructed with the z axis normal to the {110}, {112}, and {123} planes, respectively. Summarized here are the crystallographic orientations for the screw and edge FR sources, while those for the mixed-type FR sources are in-between.

	{110}	{112}	{123}
Screw	$x<112>, y<111>, z<110>$	$x<110>, y<111>, z<112>$	$x<145>, y<111>, z<123>$
Edge	$x<111>, y<112>, z<110>$	$x<111>, y<110>, z<112>$	$x<111>, y<145>, z<123>$

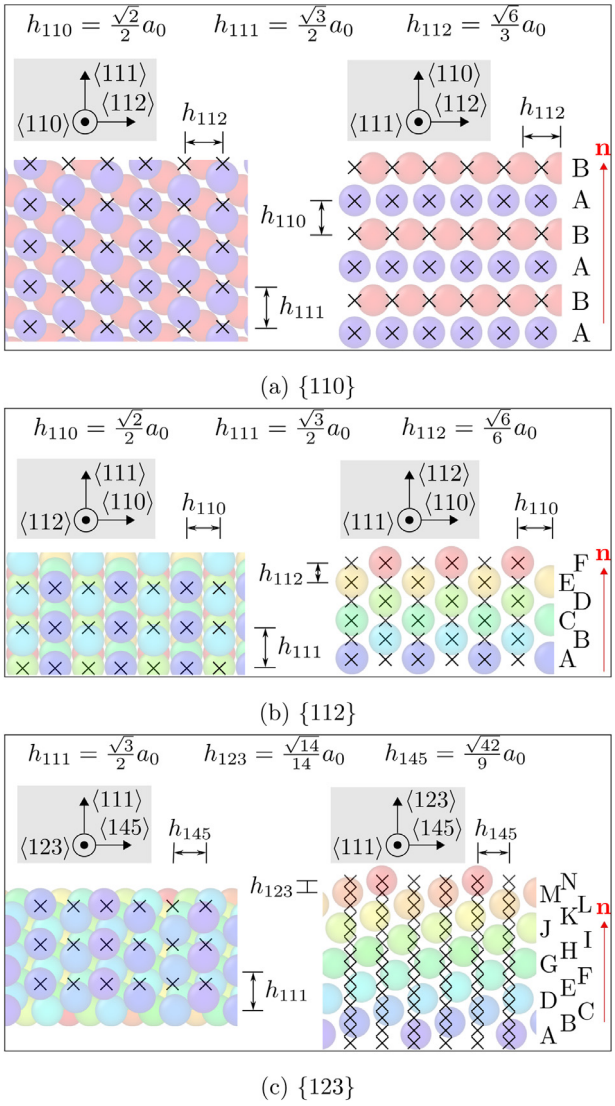

Fig. 2. Grid spacings for the three simulation cells used in PFDD simulations. Grid points are represented by black crosses. Atoms are colored based on their positions along the slip plane normal in a unit cell.

the disregistry to be comparable with that from atomistic simulation, the grid point resolution should correspond to atomic or subatomic resolution. Following a recent work (Xu et al., 2020a), grid spacings here are set to correspond to the atomic spacings and each grid point to an atomic site. Consequently, the grid spacings change with the crystallographic orientations for the screw or edge FR source, which are summarized in Table 5. For FR sources of mixed-type characters, those with character angle $\theta \leq 45^\circ$ adopt the grid spacings for the screw FR source, while those with $\theta > 45^\circ$ the grid spacings for the edge FR source. Definitions and values of the five grid spacings, h_{110}, h_{111}, h_{112}, h_{123}, and h_{145}, are illustrated in Fig. 2. As dictated by the lattice geometry, the three inter-slip-planar grid spacings differ, following $h_{110} > h_{112} > h_{123}$.

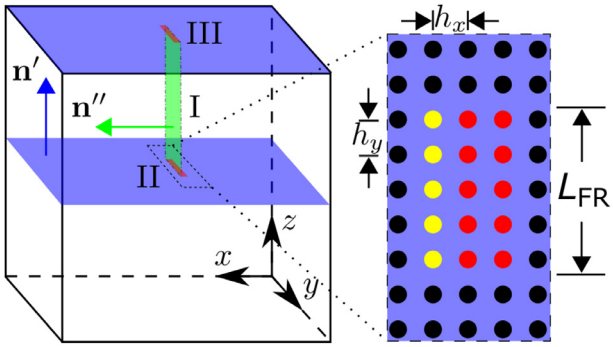

Fig. 3. An illustration of the FR source setup. Left: Two blue planes, one green plane, and three dislocation loops (I, II, and III) are involved. Right: An enlarged view of a small region on the mid-z blue plane, with each circle representing a grid point. The yellow circles constitute dislocation loop II, which lies on the intersection line between the blue and green planes. The yellow circles are assigned initial order parameter $\phi = 1$ while all other circles within the mid-z blue plane are assigned $\phi = 0$. In the simulation cell, the order parameters within the two blue planes, except those associated with the red circles, evolve following Eq. (14). (For interpretation of the references to colour in this figure legend, the reader is referred to the web version of this article.)

4.5. FR Source simulation setup

In the simulation model, the grid spacings along the x, y, and z directions are h_x, h_y, and h_z, respectively. All simulations begin with an FR source that is $L_{\mathrm{FR}} = 20h_y$ long. The FR source setup is illustrated in Fig. 3. Shown are the blue planes with their normal along the z direction and are the slip planes on which the FR source operates and, in this work, are either {110}, {112}, or {123} planes. The green plane with its normal along the x direction is not a slip plane and order parameters associated with this plane may not evolve. Some prior PF dislocation models for the FR source (e.g., Hu et al. (2004)) employ dislocation loop I in Fig. 3, which belongs solely to the green plane. With this setup, only a screw-oriented FR source for which the Burgers vector lies along the y axis can be simulated. Otherwise, parts of dislocation loop I would be prismatic. Being sessile, these parts would contribute to the elastic energy density (Eq. (10)) (Boyne et al., 2013), but not translate incurring an GSFE value (Eq. (11)). So the PFDD model presented in Section 4.1 would not be applicable. Another setup, proposed by Ruffini et al. (2017), overcomes this issue by adding two dislocation loops II/III, respectively, to the two blue planes. These two loops have an opposite Burgers vector with respect to loop I. Via dislocation reactions, the original segments of dislocation loop I located at the intersections between the blue and green planes are annihilated. The two remaining segments of dislocation loop I, which are along the z directions, may have a Burgers vector that lies out of the green plane but with no physical consequences because the associated order parameters are not within the blue planes and do not evolve (Boyne et al., 2013).

Here, the second FR source setup is employed to investigate FR sources of arbitrary dislocation character. We verified that when subject to an applied stress $\sigma_{yz}(=\sigma_{zy})$, the dislocation segment in a screw FR source on the mid-z plane bowed out toward the $+x$ direction, the same as Ruffini et al. (2017), who studied only a screw FR source. For an edge FR source, we find that the dislocation on the mid-z plane migrates toward the $-x$ direction before bowing out, as a result of its higher elastic energy than its screw counterpart. To prevent the undesirable migration, the order parameters associated with two short arrays of grid points to the right of dislocation loop II are fixed at zero during the simulation, so that the initial dislocation segment is forced to bow out toward left, i.e., the $+x$ direction (see Fig. 3). Likewise the order parameters associated with two short arrays of grid points to the left of dislocation loop III, on the top-z plane, are kept zero.

To activate the FR source, a driving resolved shear stress is applied to the system in tiny increments of $\Delta\boldsymbol{\sigma}_0 = 10^{-5}\mu^{\mathrm{H}}$. The particular shear stress component depends on the character angle of the FR source. For an edge FR source, all components of the stress tensor $\boldsymbol{\sigma}_{\mathrm{app}}$ are set to zero, except the xz and zx components, which are equal. For the screw FR source, the equal yz and zy shear components are applied, while the remaining components are zero. For the mixed character FR sources, the non-zero, equal shear components corresponding to xz, zx, yz, and zy are applied. The driving non-zero component in each case is generically denoted as σ_0. When σ_0 is increased, the dislocation starts to bow out. At a critical value, σ_{t}, the dislocation takes on a critical configuration and no longer retains the semi-elliptical shape, but beginning to expand unstably. Without the need for further increases in σ_0, the dislocation expands, folds back on itself, and forms a shear loop. The threshold value of σ_{t} for instability is used to determine the critical stress to activate the FR source which is taken to be the stress a half an increment less than the threshold, i.e., $\sigma_{\mathrm{c}} = \sigma_{\mathrm{t}} - \Delta\sigma_0/2$.

Among all material parameters used in PFDD simulations, a_0 and γ_{gsf} are based on DFT calculations, while $\boldsymbol{C}$ are taken from prior experiments (Warlimont and Martienssen, 2018). All metals are modeled with cubic elastic anisotropy, unless stated otherwise. The Ginzburg-Landau coefficient m_0 is set to unity and the timestep size is 0.02.

The elastic energy density ψ_{ela} is calculated by the fast Fourier transform method with the help of Green's functions, and hence, the simulation cell in Fig. 3 is fully periodic. To ensure that the predicted critical stress is minimally affected by the boundaries, we test operation of a screw FR source on the {110} plane in Nb for different simulation cell sizes. The

Table 6
Critical stress τ_c^H (isotropic elasticity based on the Hill average) or τ_c (anisotropic elasticity) for a screw FR source with $L_{FR} = 20b$ on a {110} plane in Nb, as a function of the number of grid points along each direction N_0. The value in the last column is calculated using Eq. (17), where $\theta = 0$, $r_0 = b$, $B = 4.26$, and an infinitely large isotropic medium is assumed.

N_0	96	128	160	192	224	256	∞
τ_c^H/μ^H	0.0732	0.0733	0.0733	0.0734	0.0734	0.0734	0.0734
τ_c/μ^H	0.0648	0.0648	0.0649	0.0649	0.0649	0.0649	

simulation cells are cubes with edge lengths along the *x*, *y*, and *z* directions denoted as L_x, L_y, and L_z, respectively. The same number of grid points N_0 is used for all three directions, i.e., $L_x = N_0 h_x$, $L_y = N_0 h_y$, and $L_z = N_0 h_z$. As shown in Table 6, as the simulation cell size N_0 decreases, so does the critical stress to activate the FR source, as a result of the attraction between the FR sources in periodic images. We find that for both elastic anisotropy and elastic isotropy cases, 256 grid points along each direction are sufficient, and thus, this simulation cell size is used in all PFDD simulations that follow.

As another form of verification, we compare the critical stress to operate the source, τ_c^H, calculated via PFDD assuming the material is elastically isotropic, with the prediction from the analytical model to activate an FR source in an isotropic linear elastic solid, given by Foreman (1967), i.e.,

$$\tau_{FO} = \left[\cos^2\left(\frac{\pi}{2} - \theta\right) + \frac{\sin^2\left(\frac{\pi}{2} - \theta\right)}{1 - \nu^H}\right] \frac{\mu^H b}{2\pi L_{FR}} \left[\ln\left(\frac{L_{FR}}{r_0}\right) + B\right] \tag{17}$$

where θ is the initial character angle of the FR source, r_0 is the dislocation core radius, and B is a non-zero term associated with the actual local curvature and size of the bow-out at its unstable point. For a screw dislocation in BCC metals, $\theta = 0$ and $r_0 = b$. We find that, when $B = 4.26$, Eq. (17) predicts the same critical stress as the PFDD simulation when Nb is modeled as an elastically isotropic medium.

5. PFDD Results

In this section, we carry out PFDD simulations of FR source operation to identify the effects of the GSFE curve shape, initial FR source character, slip plane crystallography, and elastic anisotropy on the critical stress and bow-out configuration in six BCC refractory metals.

5.1. Effects of the generalized stacking fault energy curve shape

In prior PF based models, the GSFE curve has been approximated by a $\sin^2$ function with a single peak value γ_{usf}, e.g., PFDD† (Eq. (16)) and the PF dislocation models of Wang et al. (2001) and Koslowski et al. (2002). Its form as a function of d_z is given by

$$\gamma_{gsf}(d_z) = \gamma_{usf} \sin^2\left(\frac{\pi d_z}{b}\right) \tag{18}$$

For FCC metals, Shen and Wang (2003) demonstrated the limitation of Eq. (18) function representation when modeling dislocation core-core reactions. Alternatively, the single-parameter sine function may also be considered for the GSFE curve, which follows

$$\gamma_{gsf}(d_z) = \gamma_{usf} \sin\left(\frac{\pi d_z}{b}\right) \tag{19}$$

Fig. 4 (a) directly compares the {110} GSFE curves in Mo and Nb based on direct DFT calculations, a sine function, and a $\sin^2$ function, respectively. Among the six metals studied here, Mo, a group 6 element, has the highest γ_{usf}, and Nb, a group 5 element, the lowest γ_{usf}. We observe that neither function completely fits the DFT-calculated GSFE curves of both metals. While the peak γ_{usf} is reproduced, as expected, the energies associated with displacements smaller than or larger than d_{usf}, are overestimated by the sine function and underestimated by the $\sin^2$ function.

To determine whether these small discrepancies in the GSFE representations propagate to changes in FR source operation, the critical stresses τ_c for the edge and screw FR sources on {110} planes in Mo and Nb are calculated using the GSFE curve provided by either DFT calculations, a sine function, or a $\sin^2$ function. Fig. 4(b) shows that the single-parameter GSFE approximations lead to significant errors in τ_c. The sine and $\sin^2$ functions, respectively, yield an up to 29% lower and 26.78% higher τ_c than that based on direct DFT calculations. The significant effect suggests that the energies below γ_{usf} are important in dislocation motion. To help identify key GSFE properties, we sought a function that better follows the entire GSFE curve. As shown in Fig. 4(a), the following two-parameter, two-term $\sin^2$ function provides a much better fit:

$$\gamma_{gsf}(d_z) = \gamma_{usf} \sin^2\left(\frac{\pi d_z}{b}\right) + (\gamma_{usf}/\sqrt{2} - \gamma_{qsf}) \sin^2\left(\frac{2\pi d_z}{b}\right) \tag{20}$$

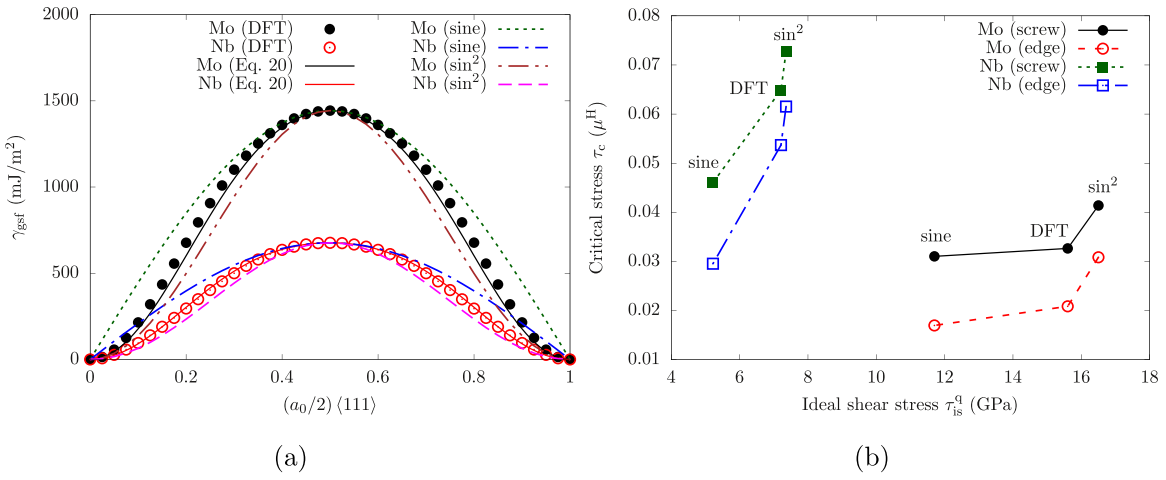

Fig. 4. (a) {110} GSFE curves in Mo and Nb based on direct DFT calculations, a two-parameter function (Eq. (20)), a sine function (Eq. (19)), and a $\sin^2$ function (Eq. (18)), respectively. (b) Critical stress τ_c (in μ^H) for a screw or an edge FR source on a {110} plane in Mo and Nb, with respect to τ_{is}^q. For each set of data, from left to right, the γ_{gsf} curves are based on a sine function, direct DFT calculations, and a $\sin^2$ function, respectively. Note that Eq. (20) and the $\sin^2$ function have the same values of τ_c and τ_{is}^q.

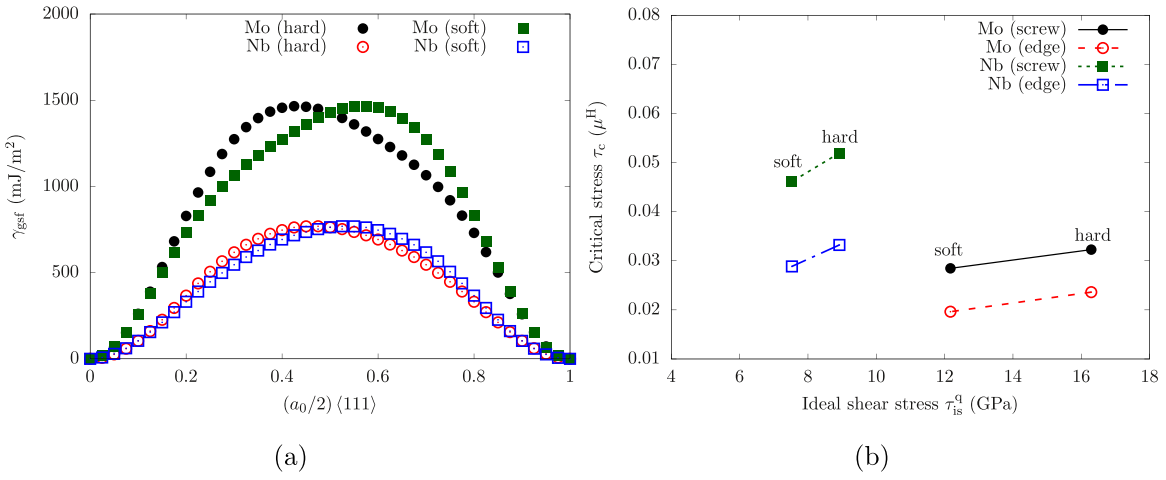

Fig. 5. (a) {112} GSFE curves in Mo and Nb based on direct DFT calculations. Curves of both hard and soft senses are shown. (b) Critical stress τ_c (in μ^H) for an FR source on a {112} plane in Mo and Nb, with respect to τ_{is}^q.

where γ_{qsf} is the GSFE value at $d_z = b/4$. The critical stresses associated with the different functions for the GSFE positively scale with τ_{is}^q, which is the value of τ_{is} at $d_z = b/4$, indicating that the energetics that impact FR source operation are associated with the smaller displacements long before d_{usf} is reached.

Unlike the {110} plane, the GSFE curves on the {112} and {123} GSFE curves are not symmetric with respect to $b/2$, making it difficult to parameterize them with a single function with a few parameters. In these cases, it is straightforward and more accurate to directly use data from direct DFT calculations.

However, the asymmetries of the {112} and {123} GSFE curves effectively correspond to two senses of directions of slip. Consider for example, the {112} GSFE curves in Mo and Nb. Fig. 5(a) compares the curves taken from Fig. 1 (circles) and those in the opposite sense (squares). The former experiences a higher γ_{qsf} value than the latter, making it a "hard" sense and the latter, the "soft" sense. In BCC metals, the two opposite $<111>$ or $<110>$ directions on {112} planes are termed twinning and antitwinning directions due to their coincidence with the twinning directions on the same planes (Weinberger et al., 2013). In terms of the Peierls stress σ_P, prior atomistic simulations for an edge dislocation in Fe have shown that σ_P along the antitwinning direction is about 1.1 times that along the twinning direction (Monnet and Terentyev, 2009).

To determine how the sense-dependence in GSFE affects FR source operation, PFDD is employed to calculate the critical stresses τ_c for the edge and screw FR sources on {112} planes in Mo and Nb in the antitwinning (hard-sense GSFE) and twinning (soft-sense GSFE) directions. Fig. 5(b) shows that like Fig. 4(b), τ_c positively scales with τ_{is}^q for the same FR source

in the same metal. FR source operation in the hard antitwinning sense leads to higher τ_c than in the soft twinning sense. Similar sense-dependence is expected to arise in FR source activation on the {123} planes, which also have asymmetric GSFE curves. Notably, these results are consistent with previously reported atomistic calculations of σ_P and may point to a contribution underlying sense sensitivity in glide of dislocations. In DDD simulations, this sense-dependence may be realized by directly using dislocation glide direction-dependent drag coefficients (Po et al., 2016).

In the remainder of the paper, for the sake of consistency, all PFDD calculations will incorporate GSFE data directly from the DFT calculations rather than parameterized functions of the GSFE curves. For the {112} and {123} planes, the GSFE curves of hard sense, i.e., those presented in Fig. 1, will be employed. Along each curve, there are 41 GSFE values, corresponding to 41 order parameter values between 0 and 1, as mentioned in Section 2. A linear interpolation scheme is used to obtain the GSFE value for an arbitrary order parameter value. The derivative of the GSFE density with respect to the order parameter, $\partial_\phi \psi_{gsf}$ (Eq. (14)), is calculated by employing the Fourier transform method (Xu et al., 2019a).

5.2. Effects of the initial character angle

With all else being the same, the screw FR source is expected to be harder to activate than the edge FR source, since the former involves creating edge dislocation lines in the bow-out process and for an isotropic material like W, it has the highest elastic energy among all orientations. Based on the elastic energy alone, Eq. (17) predicts that in an elastically isotropic medium, the ratio in the critical stress between a screw FR source and an edge one is $1/(1-\nu^H)$, independent of the initial FR source length L_{FR}. DDD simulations for elastically isotropic (Bacon, 1967) or anisotropic materials (Bacon et al., 1973) recover this result. In this section, we first examine the effect of initial orientation of the FR source segment using PFDD, which accounts for not only the elastic energy but also the inter-slip-planar energy.

We first model FR source operation on the {110} planes in W, in order to naturally investigate bow-out configurations without the effects of elastic anisotropy. Fig. 6 presents the FR source configurations for the entire range of dislocation character, from the screw source (character angle $\theta = 0^\circ$), to mixed character sources, $\theta = 15^\circ$, 30°, 45°, 60°, and 75°, and finally to the edge source ($\theta = 90^\circ$). These stretched dislocations correspond to those after 10,000 timesteps, when the system is subject to an applied stress of $1.01\tau_c$, just above the corresponding critical stress. To achieve these configurations, the distances the dislocation have slipped are on the order of L_{FR}. Therefore, each case in Fig. 6 spans a small area on the glide plane in order to zoom in on critical bow-out shape. The extent propagated and shape of the critical bow-out configurations are sensitive to the initial FR source character. The bow-out for the screw FR source is the smallest, less than $L_{FR}/2$. Then it increases progressively as the initial character adopts a larger edge component. For the mixed source ($\theta = 30^\circ$), the bow-out expands to nearly $L_{FR}/2$. The edge source achieves the largest bow-out before becoming unstable, extending close to but still less than L_{FR}.

The shapes of these configurations are also affected by the initial FR source character. For all cases in W, the bow-out takes on a shape that will minimize the edge parts and maximize the screw parts of the half loop. For the screw FR source, for example, the bow-out configuration is oblong, a shape that maximizes the length of the low-energy screw segment. The radius of curvature of the bow-out is relatively large. For the edge source, the situation is reversed: the bow-out is approximately semi-circular with a small radius of curvature, effectively minimizing the length of edge portions. For all mixed-type FR sources, the bow-out shape is asymmetric. The bow out is skewed to maximize the portion of the dislocation line that has screw character which has the lowest elastic energy.

Next, we study the critical stresses to activate the sources τ_c. To assess all six metals, τ_c as a function of the initial line character of the FR source are shown in Fig. 7(a). To minimize influences of elasticity in this comparison, these critical stresses are normalized by their corresponding isotropic equivalent shear modulus μ^H. In all six metals, the screw-oriented FR source has the highest τ_c. In four of the six metals, i.e., Mo, Ta, V, and W, τ_c decreases monotonically with increases in the character angle θ from pure screw (0°) to pure edge (90°). For Cr and Nb, τ_c attains a second peak at $\theta = 45^\circ$. These two metals have the lowest elastic anisotropic index A_c among the six refractory metals and hence the most severe departure from the idealized isotropic elastic behavior. To remove the influence of elastic anisotropy, we re-calculated the critical activation stresses for all six metals, employing their elastic isotropic equivalent constants instead. The stresses, denoted as τ_c^H, are presented in Fig. 7(b). For all metals, including Cr and Nb, τ_c^H decreases monotonically from the screw-oriented source to the edge-oriented source. The variation of τ_c^H with θ generally follows

$$\tau_c^H(\theta) = \frac{1}{2}\left[\tau_{c,edge}^H + \tau_{c,screw}^H - (\tau_{c,edge}^H - \tau_{c,screw}^H)\cos(2\theta)\right]. \tag{21}$$

These results identify the low $A_c < 1$ as a possible reason that a locally maximum τ_c is achieved at $\theta = 45^\circ$, suggesting that this phenomenon may arise from that anisotropy has altered the orientation dependence of the elastic energy. To determine the effect of anisotropy on the elastic energy, PFDD calculations of seven straight dislocations, each of which is with one of the seven character angles, are carried out in all six BCC metals, assuming either elastically anisotropy or isotropy. Simulation details are presented in Appendix B and the results are summarized in Fig. B.1 showing plots of elastic energy subtracted from that for the screw dislocation in an anisotropic medium (so larger negative values mean larger elastic energy). It is shown that apart from the screw orientation, the percent increase in the elastic energy due to elastic anisotropy for all character angles is the largest for Cr and Nb. In other metals, such as Mo and V, the anisotropy-induced enhancements are comparatively smaller than those for Cr and Nb. For Ta, notably, the only metal with $A_c > 1$ studied here,

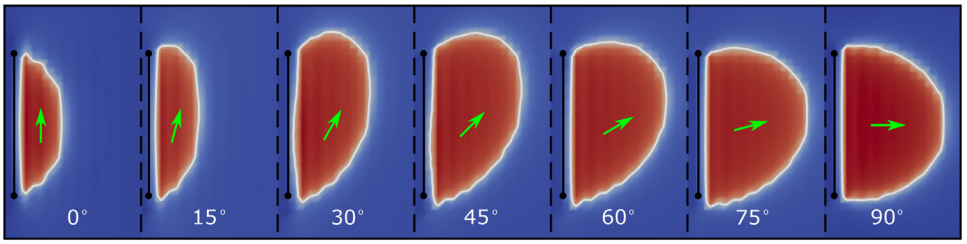

Fig. 6. Snapshots of configurations of FR sources of pure and mixed-type characters on {110} planes in W at 10,000 timesteps when the system is subject to an applied stress of $1.01\tau_c$. All snapshots are colored by the disregistry ξ (Eq. (15)), where blue and red correspond to $\xi = 0$ and b, respectively. The white curves, indicating dislocations, are contour lines on which $\xi = b/2$. In each snapshot, the green arrow indicates the direction of the Burgers vector. (For interpretation of the references to colour in this figure legend, the reader is referred to the web version of this article.)

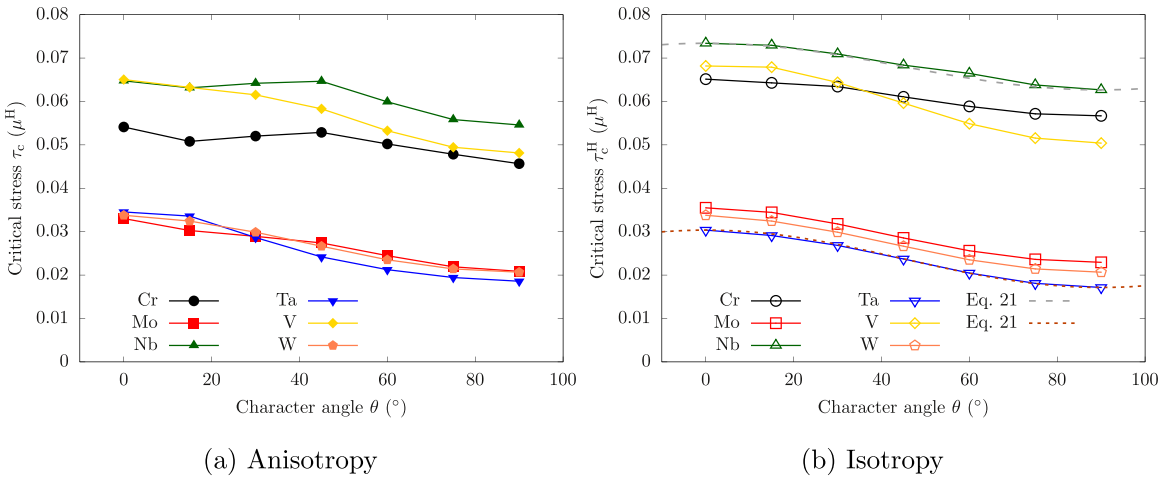

Fig. 7. The critical stress of FR sources on {110} planes in six BCC metals, assuming (a) elastically anisotropic and (b) elastically isotropic, respectively. Note that W is an elastically isotropic material.

anisotropy leads to a decrease. Evidently, in bowing out the 45°-oriented FR source, additional dislocation lengths are created that are much more energetically costly for Nb and Cr than for the other metals due to their large sub-unity departure from isotropy, $A_c < 1$, or equivalently relatively low C_{44} modulus compared to the $(C_{11} - C_{12})/2$ modulus.

As a testament of the many factors that affect the FR source operation, the critical stresses predicted here do not follow the same trends as the GSFE values. The normalized critical stresses τ_c/μ^H can be divided into two groups, with the Nb, Cr, and V, metals exhibiting higher τ_c/μ^H than the remaining metals Mo, Ta, and W. These are not divided by groups in the periodic table and they do not scale with the peak GSFE value γ_{usf} or the ideal shear strength T_{is}.

5.3. FR Source operation on different glide planes

Dislocations in BCC metals can glide on multiple types of slip planes, not only the {110} planes, but also two higher order planes, {112} and {123} planes. The changes in the critical stress and bow-out configuration when the same FR source lies on different glide planes could lend insight into slip system activation. As in Fig. 6, Fig. 8 compares the critical bow-out configurations of the FR source for W at 10,000 timesteps, when the system is subject to an applied stress of $1.01\tau_c$. For the same type of FR source, the bow-out configuration on the {123} planes is the largest with the smallest radius of curvature, then the {112} plane with a smaller bow-out, and the least on the {110} plane with the smallest bow-out. The difference in the radii of curvature of the bow out configurations on different slip planes roughly scales with their different critical stresses τ_c. On all glide planes, for the edge-oriented FR source, extent of the bow-out is over $L_{FR}/2$, whereas for the screw-oriented FR source, the bow-out is less than $L_{FR}/2$.

Next, we analyse the screw FR source configuration in the metals that have the two most extreme elastic anisotropy: Nb and Ta, which have the lowest (0.5027) and highest (1.5585) elastic anisotropy indices, respectively. Fig. 9 presents the bow-out configurations of a screw FR source in these two metals. Similar to the case of W, at the critical point, the bow out of the FR source segment on the {123} plane is larger than that on the {112} plane. The critical bow out for both {112} and {123} FR sources are much larger than that on the {110} plane. The shape of the segments on the {112} and {123} planes have a larger radius of curvature, which often translates to lower critical stresses on these planes. As anticipated, on all slip planes, the non-screw portions are minimized in each bow-out configuration.

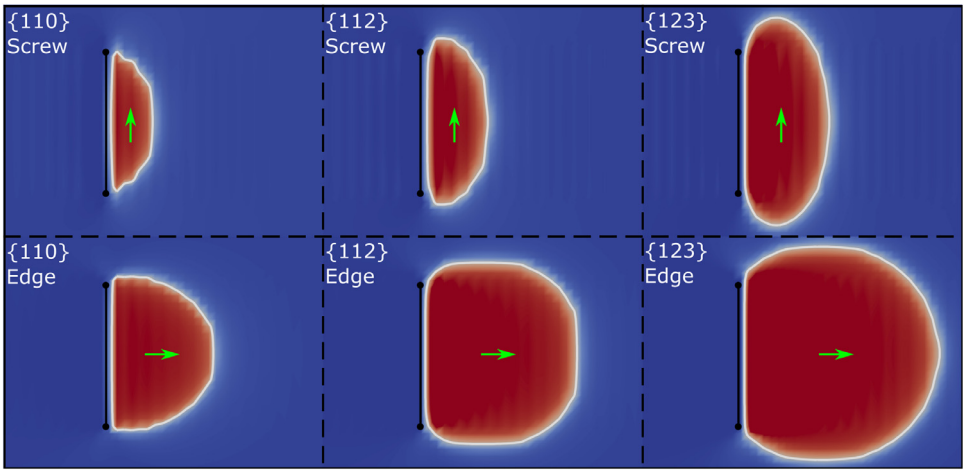

Fig. 8. Snapshots of FR source configurations in W at 10,000 timesteps when the system is subject to an applied stress of $1.01\tau_c$. All snapshots are colored in the same way as Fig. 6.

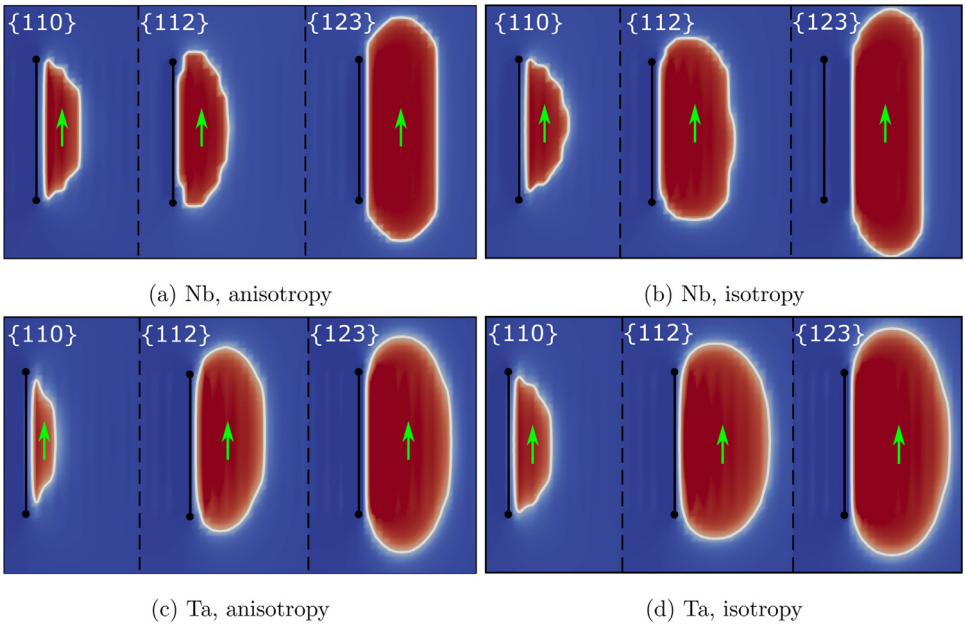

Fig. 9. Snapshots of a screw FR source configuration in Nb and Ta at 10,000 timesteps when the system is subject to an applied stress of $1.01\tau_c$. All snapshots are colored in the same way as Fig. 6.

Fig. 9 also presents FR source configurations when assuming the metals have the effective elastic isotropic constants. Removing elastic anisotropy is found to increase the extent of the bow-out of the FR source, but does not change the overall shape and symmetry of the configuration. This finding holds for both Nb ($A_c < 1$) and Ta ($A_c > 1$). The effect for Ta is similar to that reported for Fe ($A_c = 7.4436$). Prior DDD simulations (Aubry et al., 2011) found that, in an isotropic medium, a dislocation loop on a {111} plane protrudes more along the Burgers vector direction than that in an anisotropic medium.

Fig. 10 compares the critical stresses τ_c among three slip planes, {110}, {112}, and {123}, in all six metals. As before, these stresses are normalized by their corresponding isotropic equivalent shear modulus. τ_c exhibits a significant dependency on the plane on which the FR source operates. The spread in the critical stress among the three planes is generally higher for metals with $A_c < 1$ (Cr, Mo, Nb, and V) than with $A_c \geq 1$ (W and Ta). The hardest FR sources lie on the {110} plane and the easiest FR sources to activate on the {123} plane. Slight exceptions are Mo and W, where the critical stresses to activate sources on the {110} and {112} planes are similar. These results do not change qualitatively when the effective isotropic constants are used instead of the actual anisotropic ones.

Fig. 11 shows the ratios of the critical stress of the screw FR source to that of the edge FR source, while assuming elastic isotropy. These ratios are greater than unity, ranging from 1.15 for Nb ($A_c = 0.5027$) to 2.22 for Ta ($A_c = 1.5585$). For

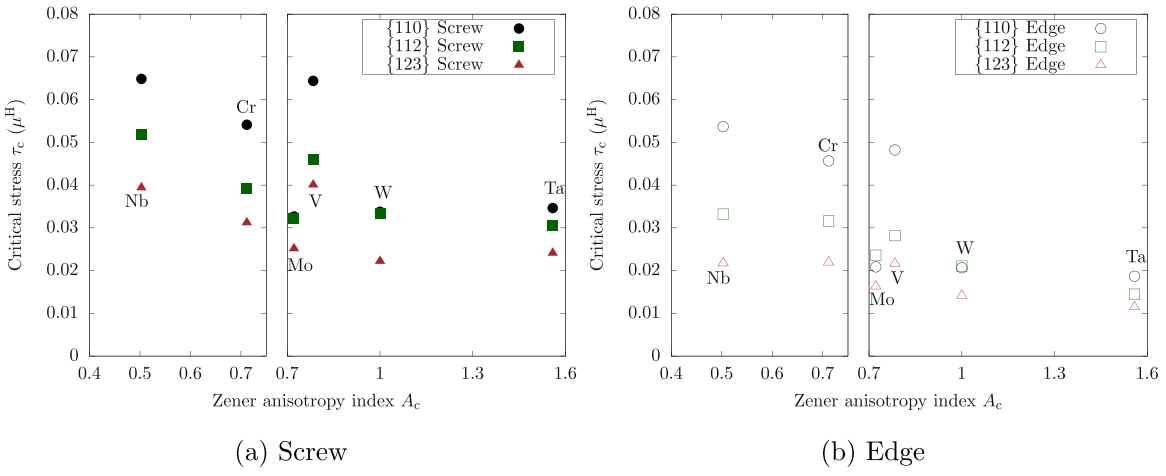

Fig. 10. The critical stress τ_c of (a) a screw and (b) an edge FR source on three slip planes in six BCC metals.

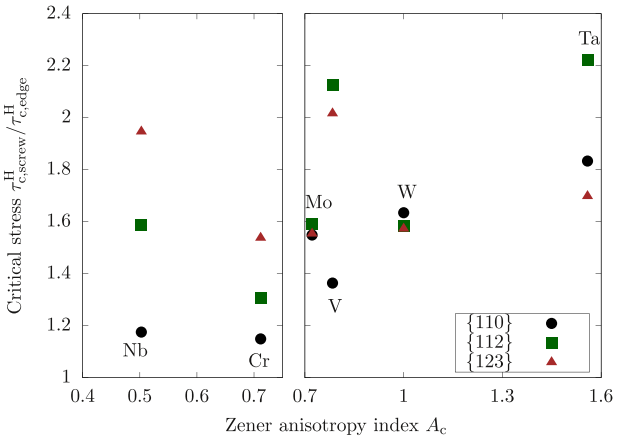

Fig. 11. For edge and screw FR sources in six BCC metals, assuming elastic Hill average, the ratio of the critical stress of the screw FR source to that of the edge FR source.

elastically isotropic materials, the analytical model Eq. (17) predicts that the ratio is $1/(1-\nu^H)$, which for the metals here ranges only from 1.25 to 1.67. The greater screw-edge differences predicted by PFDD can be attributed to paired dislocation interactions and other material specific properties, such as the GSFE curves.

The two higher order planes, {112} and {123}, are worth a closer examination. For the same metal, the shapes of the GSFE curves on the two planes are nearly identical, with the difference in γ_{usf} less than 3%. Hence, while assuming elastic isotropy, any difference in critical stress and bow-out configuration between the two planes may be mainly attributed to the differences in the inter-slip-planar spacing, which affects the balance between the elastic energy and GSFE. Fig. 12 shows the ratios $\tau^H_{c,112}/\tau^H_{c,123}$ for the two types of FR sources in all six BCC metals. Except for an edge FR source in Nb (1.71), all critical stress ratios fall into a narrow range between 1 and 1.5. The finding that this ratio is not unity highlights the effects of the slip plane crystallography.

5.4. *Effects of the elastic anisotropy*

Many of the FR source critical stresses and bow-out configurations presented thus far have demonstrated a strong effect of elastic anisotropy. Here, we examine the anisotropic effect across all metals by analyzing in Fig. 13 the ratio of the anisotropic to isotropic critical stresses with respect to the anisotropy index A_c. For most of the cases (30 out of 36), elastic anisotropy reduces the critical stress when $A_c < 1$, and enhances the critical stress when $A_c > 1$. Exceptions include the operation of edge FR sources in Cr and V on the {112} and {123} planes. Although $A_c < 1$ for these two metals, elastic anisotropy enhances the critical stress to operate the FR sources. Yet still, the stress to operate the screw sources is reduced in Cr and V. The only two other exceptions are the edge FR source on {112} plane in Mo and that on {123} plane in Ta. In Nb, which

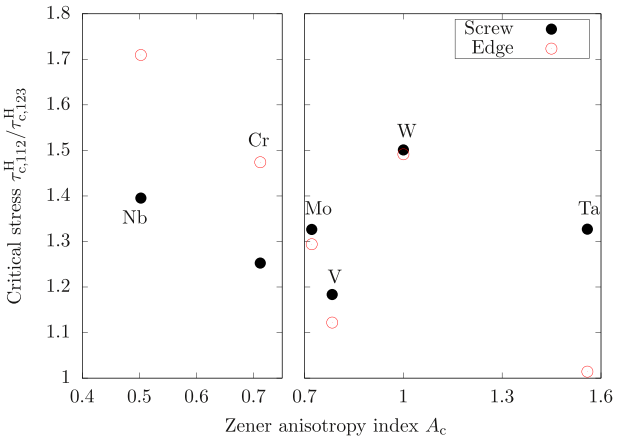

Fig. 12. For edge and screw FR sources in six BCC metals, assuming elastic Hill average, the ratio of the critical stress on the {112} plane to that on the {123} plane.

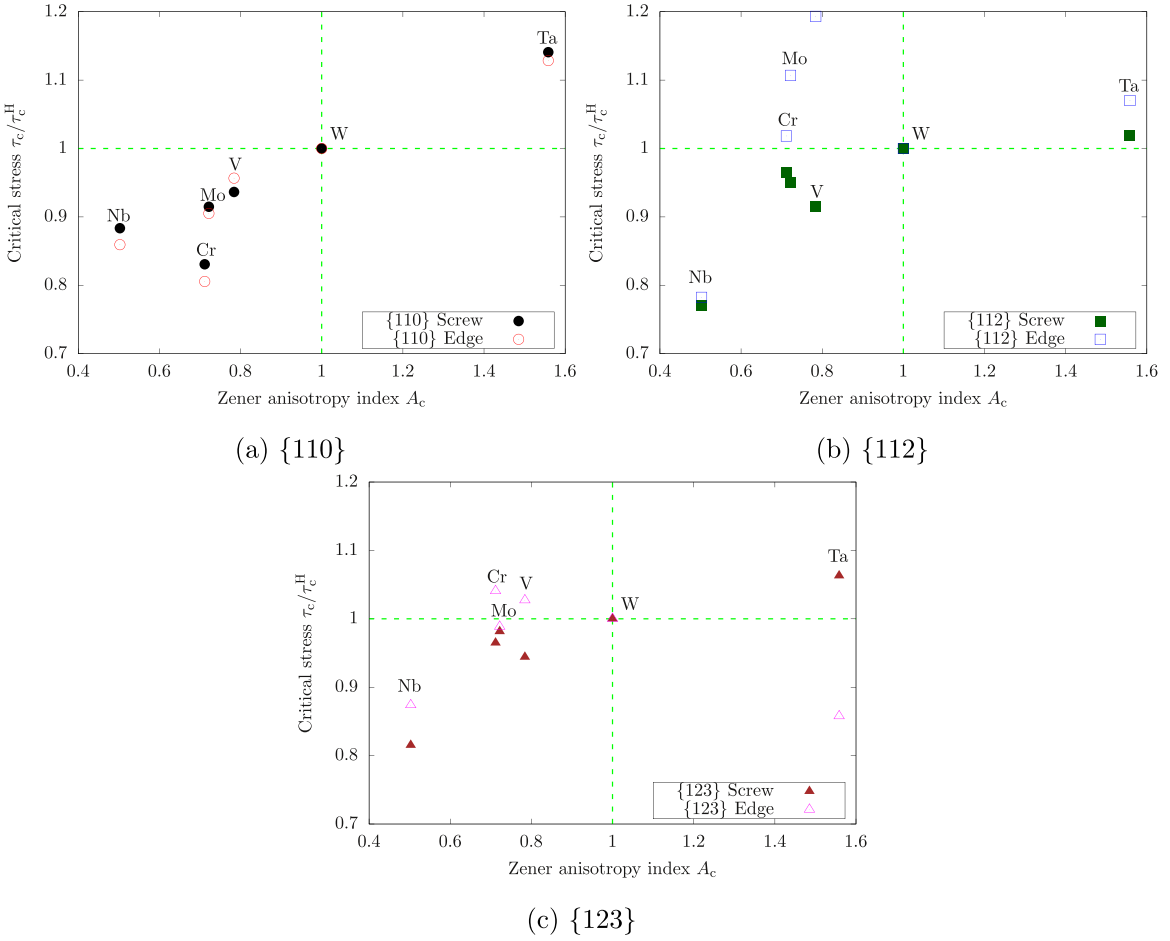

Fig. 13. For edge and screw FR sources in six BCC metals, the ratio of the elastic anisotropy-based critical stress τ_c to elastic isotropic Hill average-based one τ_c^H.

has the lowest A_c, the reduction in the critical stress is much more pronounced for the {112} and {123} planes than on the {110} plane. In Ta, which possess the highest A_c, the enhancement in the critical stress is more significant for the {110} planes than for the other two planes. Overall, the results demonstrate that neglecting elastic ansiotropy can lead to serious errors in the estimates for the stresses required to operate FR sources.

It is worth noting that the effects of the elastic anisotropy on the FR source critical stress demonstrated here differ from the ones reported earlier. In a previous DDD simulation on both {110} and {112} slip planes in BCC Fe at 912°C ($A_c = 7.4436$), assuming elastic isotropy (using Voigt or Reuss averages) resulted in an overestimation and underestimation of the critical stress for the edge and screw FR sources, respectively (Fitzgerald et al., 2012). Isolating the sources of the differences are not straightforward since first of all, the materials are different and Fe is not studied here. In addition, there exist a plethora of differences between PFDD and DDD approaches, as discussed in Section 4.3.

6. Conclusions

In this work, we use PFDD to study the activation of dislocation FR sources in six BCC refractory metals (Cr, Mo, Nb, Ta, V, and W), which vary widely in their anisotropic elastic properties and GSFE values. We consider FR sources that are initially pure screw, to mixed, and to pure edge and operate on three types of slip planes: {110}, {112}, and {123}. From the simulations, we analyze the critical stress to activate the FR source and the dislocation bow-out configuration, as a function of the GSFE curve shape, initial FR source character angle, slip plane crystallography, and elastic anisotropy. To the best of our knowledge, this is the first time a PF dislocation model has been applied in BCC crystals to study activation of (i) FR sources and (ii) dislocation glide on non-110 glide planes. The main results are summarized as follows:

1. Among the six BCC metals, DFT calculations show that the group 6 elements (Cr, Mo, and W) have a higher shear modulus, a lower Poisson's ratio, a higher ideal shear strength, and higher GSFEs than the group 5 elements (Nb, Ta, and V).
2. For Cr, neglecting antiferromagnetism results in an underestimation of the lattice parameter a_0, as well as an overestimation of the isotropic Poisson's ratio ν^{H}, GSFEs, and the ideal shear strength. Note that considering antiferromagnetism in Cr brings the predicted results of a_0 and ν^{H} closer to the experimental values.
3. The {110} GSFE curves, while symmetric, cannot be well approximated by a sine or a $\sin^2$ function as conventionally used. A newly proposed two-parameter, two-term $\sin^2$ function is shown to more accurately model the GSFE curves for the {110} slip plane.
4. The {112} and {123} GSFE curves are asymmetric. As a result, each curve has two senses: hard and soft. PFDD simulations with curves of hard and soft senses, respectively, predict a higher and lower critical stress for the same FR source in the same metal.
5. The configurations of the FR sources of edge and screw type on all three slip planes are symmetric, while those of mixed-type on the {110} slip plane are asymmetric.
6. For all six metals, the edge FR source configurations are much more extended compared to the screw FR source. In addition, for the same FR source character angle in the same metal, the bow-out on the {123} planes is the largest, then the {112} plane, and on the {110} plane the smallest.
7. Approximating an elastically anisotropic medium as an isotropic one results in an overestimation and an underestimation of the critical stress for the FR sources, respectively, when the anisotropy index A_c is smaller than and larger than unity. For the FR source configuration, the dislocation bow-out becomes more extended when a material is approximated as elastically isotropic, regardless of the value of A_c.
8. For both Cr and Nb, which possess the lowest elastic anisotropy indices among the six metals, elastic anisotropy causes the critical stress to activate FR sources on the {110} plane to achieve a local maximum at the 45° character angle.

Declaration of Competing Interest

We declare no conflict of interest.

CRediT authorship contribution statement

Shuozhi Xu: Conceptualization, Methodology, Software, Formal analysis, Resources, Data curation, Writing - original draft, Writing - review & editing, Visualization. **Yanqing Su:** Methodology, Software, Formal analysis, Data curation, Writing - original draft, Writing - review & editing. **Lauren T. W. Smith:** Methodology, Software, Validation, Writing - review & editing. **Irene J. Beyerlein:** Conceptualization, Resources, Writing - review & editing, Supervision, Funding acquisition.

Acknowledgements

We thank Dr. Abigail Hunter and Dr. Xiangguo Li for helpful discussions. The work of SX was supported in part by the Elings Prize Fellowship in Science offered by the California NanoSystems Institute (CNSI) on the UC Santa Barbara campus. LS acknowledges support from the Department of Energy National Nuclear Security Administration Stewardship Science Graduate Fellowship. The authors gratefully acknowledge support from the Office of Naval Research under contract ONR BRC Grant N00014-18-1-2392. Use was made of computational facilities purchased with funds from the National Science Foundation (CNS-1725797) and administered by the Center for Scientific Computing (CSC). The CSC is supported by the CNSI

and the Materials Research Science and Engineering Center; (MRSEC NSF DMR 1720256) at UC Santa Barbara. This work used the Extreme Science and Engineering Discovery Environment (XSEDE), which is supported by National Science Foundation grant number ACI-1053575.

Appendix A. Positions of atoms in simulation cells for GSFE calculations

Appendix B. Elastic energy of straight dislocations on a {110} plane

A dislocation dipole consisting of two dislocations of the same type but with opposite Burgers vector is built into a 3D periodic simulation cell, following our recent work (Xu et al., 2019b, 2019c). Seven character angles θ are considered, including 0° (screw), 15°, 30°, 45°, 60°, 75°, and 90° (edge). The two dislocation lines lie on the mid-z plane along the y axis and are separated by $L_x/2$ along the x direction. The z axis is along the $<110>$ direction and all other simulation parameters are the same as those for the {110} FR source simulations for the same θ. It follows that total energy of the dislocated system is minimized and the relaxed elastic energy of a single dislocation is presented in Fig. B.1.

Table A.1
Positions of six atoms in a unit cell for the {110} plane GSFE curves calculations. The crystallographic orientations are $x[11\bar{2}]$, $y[\bar{1}10]$, and $z[111]$.

Atom	x (in $\sqrt{6}a_0$)	y (in $\sqrt{2}a_0$)	z (in $\sqrt{3}a_0/2$)
1	0	0	0
2	2/6	0	1/3
3	4/6	0	2/3
4	1/6	1/2	2/3
5	3/6	1/2	0
6	5/6	1/2	1/3

Table A.2
Positions of six atoms in a unit cell for the {112} plane GSFE curves calculations. The crystallographic orientations are $x[1\bar{1}0]$, $y[11\bar{2}]$, and $z[111]$.

Atom	x (in $\sqrt{2}a_0$)	y (in $\sqrt{6}a_0$)	z (in $\sqrt{3}a_0/2$)
1	0	0	0
2	0	2/6	1/3
3	0	4/6	2/3
4	1/2	1/6	2/3
5	1/2	3/6	0
6	1/2	5/6	1/3

Table A.3
Positions of 42 atoms in a unit cell for the {123} plane GSFE curves calculations. The crystallographic orientations are $x[5\bar{4}1]$, $y[12\bar{3}]$, and $z[111]$.

Atom	x (in $\sqrt{42}a_0$)	y (in $\sqrt{14}a_0$)	z (in $\sqrt{3}a_0/2$)
1	0	0	0
2	14/42	0	2/3
3	28/42	0	1/3
4	5/42	1/14	2/3
5	19/42	1/14	1/3
6	33/42	1/14	0
7	10/42	2/14	1/3
8	24/42	2/14	0
9	38/42	2/14	2/3
10	1/42	3/14	1/3
11	15/42	3/14	0
12	29/42	3/14	2/3
13	6/42	4/14	0
14	20/42	4/14	2/3
15	34/42	4/14	1/3
16	11/42	5/14	2/3
17	25/42	5/14	1/3
18	39/42	5/14	0
19	2/42	6/14	2/3
20	16/42	6/14	1/3
21	30/42	6/14	0
22	7/42	7/14	1/3
23	21/42	7/14	0
24	35/42	7/14	2/3
25	12/42	8/14	0
26	26/42	8/14	2/3
27	40/42	8/14	1/3
28	3/42	9/14	0
29	17/42	9/14	2/3
30	31/42	9/14	1/3
31	8/42	10/14	2/3
32	22/42	10/14	1/3
33	36/42	10/14	0
34	13/42	11/14	1/3
35	27/42	11/14	0
36	41/42	11/14	2/3
37	4/42	12/14	1/3
38	18/42	12/14	0
39	32/42	12/14	2/3
40	9/42	13/14	0
41	23/42	13/14	2/3
42	37/42	13/14	1/3

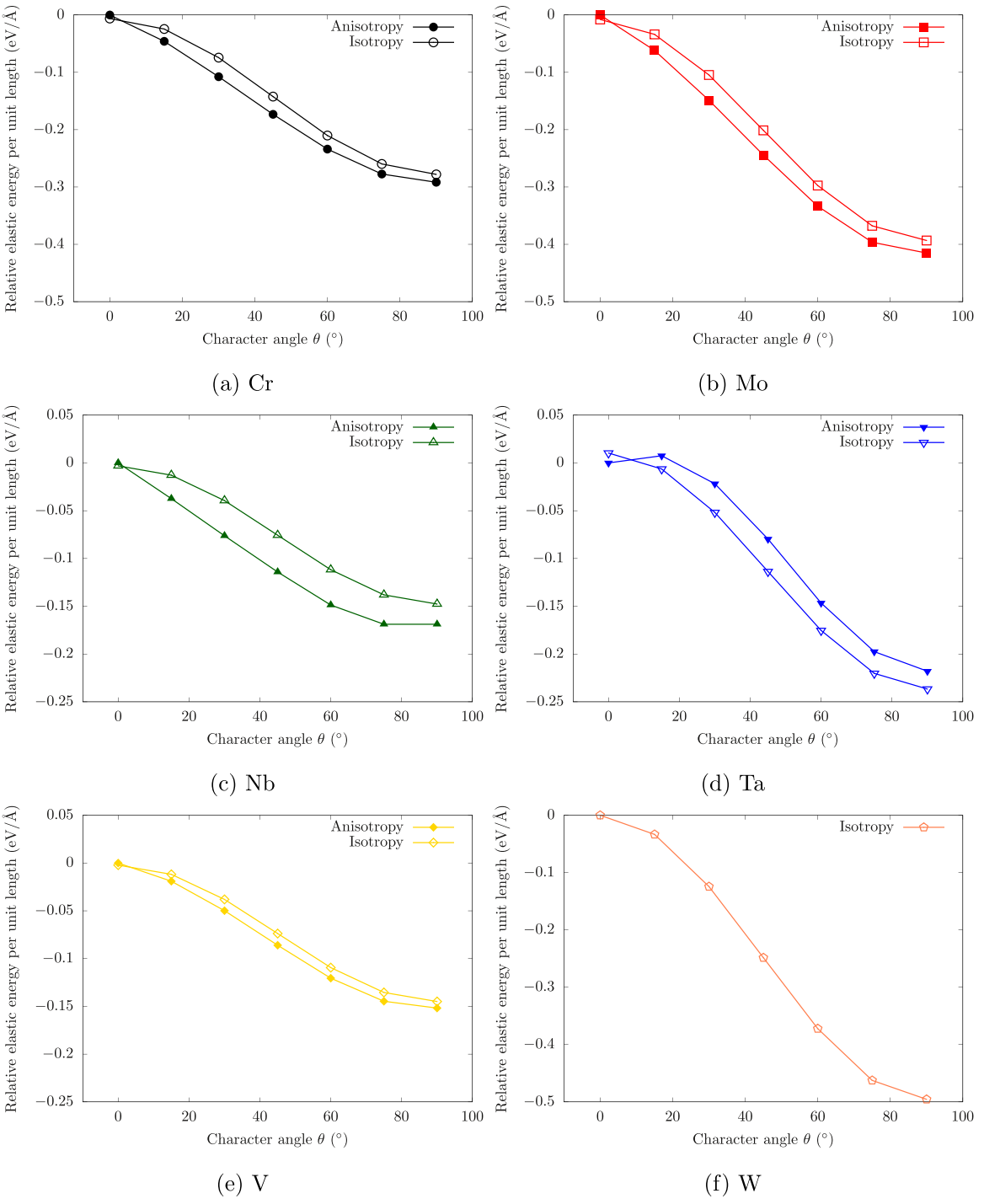

Fig. B.1. Dependence of the relaxed relative elastic energy of a single dislocation per unit length in six BCC metals. In each metal, the elastic energy relative to the corresponding value of a screw dislocation in an anisotropic medium is presented, so larger negative values mean larger elastic energy. Note that W is an elastically isotropic material.

References

Anciaux, G., Junge, T., Hodapp, M., Cho, J., Molinari, J.F., Curtin, W.A., 2018. The Coupled Atomistic/Discrete-Dislocation method in 3d part I: Concept and algorithms. J. Mech. Phys. Solids 118, 152–171. doi:10.1016/j.jmps.2018.05.004.

Anderson, P.M., Hirth, J.P., Lothe, J., 2017. Theory of Dislocations, 3rd edition Cambridge University Press, Cambridge.

Aubry, S., Fitzgerald, S.P., Dudarev, S.L., Cai, W., 2011. Equilibrium shape of dislocation shear loops in anisotropic α-Fe. Modelling Simul. Mater. Sci. Eng. 19 (6), 065006. doi:10.1088/0965-0393/19/6/065006.

Bacon, D.J., 1967. A method for describing a flexible dislocation. Phys. Stat. Sol. (b) 23 (2), 527–538. doi:10.1002/pssb.19670230212.

Bacon, D.J., Kocks, U.F., Scattergood, R.O., 1973. The effect of dislocation self-interaction on the Orowan stress. Philos. Mag. 28 (6), 1241–1263. doi:10.1080/14786437308227997.

Berry, J., Provatas, N., Rottler, J., Sinclair, C.W., 2012. Defect stability in phase-field crystal models: Stacking faults and partial dislocations. Phys. Rev. B 86 (22), 224112. doi:10.1103/PhysRevB.86.224112.

Berry, J., Provatas, N., Rottler, J., Sinclair, C.W., 2014. Phase field crystal modeling as a unified atomistic approach to defect dynamics. Phys. Rev. B 89 (21), 214117. doi:10.1103/PhysRevB.89.214117.

von Blanckenhagen, B., Gumbsch, P., Arzt, E., 2003. Dislocation sources and the flow stress of polycrystalline thin metal films. Philos. Mag. Lett. 83 (1), 1–8. doi:10.1080/0950083021000050287.

Blöchl, P.E., 1994. Projector augmented-wave method. Phys. Rev. B 50 (24), 17953–17979. doi:10.1103/PhysRevB.50.17953.

Bonny, G., Terentyev, D., Bakaev, A., Grigorev, P., Neck, D.V., 2014. Many-body central force potentials for tungsten. Modelling Simul. Mater. Sci. Eng. 22 (5), 053001. doi:10.1088/0965-0393/22/5/053001.

Boyne, A., Shen, C., Najafabadi, R., Wang, Y., 2013. Numerical simulation of irradiation hardening in Zirconium. J. Nucl. Mater. 438 (1), 209–217. doi:10.1016/j.jnucmat.2013.03.035.

Brandl, C., Derlet, P.M., Van Swygenhoven, H., 2007. General-stacking-fault energies in highly strained metallic environments: *Ab initio* calculations. Phys. Rev. B 76 (5), 054124. doi:10.1103/PhysRevB.76.054124.

Chavoshi, S.Z., Xu, S., 2019. Nanoindentation/scratching at finite temperatures: Insights from atomistic-based modeling. Prog. Mater. Sci. 100, 1–20. doi:10.1016/j.pmatsci.2018.09.002.

Chen, D., Xu, S., Kulkarni, Y., 2020. Atomistic mechanism for vacancy-enhanced grain boundary migration. Phys. Rev. Mater. 4 (3), 033602. doi:10.1103/PhysRevMaterials.4.033602.

Cho, J., Molinari, J.-F., Curtin, W.A., Anciaux, G., 2018. The coupled atomistic/discrete-dislocation method in 3d. Part III: Dynamics of hybrid dislocations. J. Mech. Phys. Solids 118, 1–14. doi:10.1016/j.jmps.2018.05.005.

Dezerald, L., Ventelon, L., Clouet, E., Denoual, C., Rodney, D., Willaime, F., 2014. *Ab initio* modeling of the two-dimensional energy landscape of screw dislocations in bcc transition metals. Phys. Rev. B 89 (2), 024104. doi:10.1103/PhysRevB.89.024104.

Edagawa, K., Kamimura, Y., Iskandarov, A.M., Umeno, Y., Takeuchi, S., 2019. Peierls stresses estimated by a discretized Peierls-Nabarro model for a variety of crystals. Materialia 5, 100218. doi:10.1016/j.mtla.2019.100218.

Elder, K.R., Katakowski, M., Haataja, M., Grant, M., 2002. Modeling elasticity in crystal growth. Phys. Rev. Lett. 88 (24), 245701. doi:10.1103/PhysRevLett.88.245701.

Elder, K.R., Provatas, N., Berry, J., Stefanovic, P., Grant, M., 2007. Phase-field crystal modeling and classical density functional theory of freezing. Phys. Rev. B 75 (6), 064107. doi:10.1103/PhysRevB.75.064107.

Fitzgerald, S.P., 2010. Frank-Read sources and the yield of anisotropic cubic crystals. Philos. Mag. Lett. 90 (3), 209–218. doi:10.1080/09500830903571392.

Fitzgerald, S.P., Aubry, S., Dudarev, S.L., Cai, W., 2012. Dislocation dynamics simulation of Frank-Read sources in anisotropic α-Fe. Modelling Simul. Mater. Sci. Eng. 20 (4), 045022. doi:10.1088/0965-0393/20/4/045022.

Foreman, A.J.E., 1967. The bowing of a dislocation segment. Philos. Mag. 15 (137), 1011–1021. doi:10.1080/14786436708221645.

Frank, F.C., Read, W.T., 1950. Multiplication processes for slow moving dislocations. Phys. Rev. 79 (4), 722–723. doi:10.1103/PhysRev.79.722.

Frederiksen, S.L., Jacobsen, K.W., 2003. Density functional theory studies of screw dislocation core structures in bcc metals. Philos. Mag. 83 (3), 365–375. doi:10.1080/0141861021000034568.

Gurrutxaga-Lerma, B., Balint, D.S., Dini, D., Sutton, A.P., 2015. The mechanisms governing the activation of dislocation sources in aluminum at different strain rates. J. Mech. Phys. Solids 84, 273–292. doi:10.1016/j.jmps.2015.08.008.

Hill, R., 1952. The elastic behaviour of a crystalline aggregate. Proc. Phys. Soc. A 65 (5), 349–354. doi:10.1088/0370-1298/65/5/307.

Hodapp, M., Anciaux, G., Molinari, J.F., Curtin, W.A., 2018. Coupled atomistic/discrete dislocation method in 3d Part II: Validation of the method. J. Mech. Phys. Solids 119, 1–19. doi:10.1016/j.jmps.2018.05.003.

Hu, S.Y., Li, Y.L., Zheng, Y.X., Chen, L.Q., 2004. Effect of solutes on dislocation motion — a phase-field simulation. Int. J. Plast. 20 (3), 403–425. doi:10.1016/S0749-6419(03)00094-9.

Huang, M.-S., Zhu, Y.-X., Li, Z.-H., 2014. Dislocation dissociation strongly influences on Frank-Read source nucleation and microplasticy of materials with low stacking fault energy. Chin. Phys. Lett. 31 (4), 046102. doi:10.1088/0256-307X/31/4/046102.

Hull, D., Bacon, D.J., 2011. Introduction to Dislocations, 5th Butterworth-Heinemann.

Hunter, A., Beyerlein, I.J., 2015. Relationship between monolayer stacking faults and twins in nanocrystals. Acta Mater. 88, 207–217. doi:10.1016/j.actamat.2014.12.045.

Kang, K., Bulatov, V.V., Cai, W., 2012. Singular orientations and faceted motion of dislocations in body-centered cubic crystals. Proc. Natl. Acad. Sci. USA 109 (38), 15174–15178. doi:10.1073/pnas.1206079109.

Kittel, C., 2004. Introduction to Solid State Physics, 8th edition Wiley, Hoboken, NJ.

de Koning, M., Cai, W., Bulatov, V.V., 2003. Anomalous dislocation multiplication in FCC metals. Phys. Rev. Lett. 91 (2), 025503. doi:10.1103/PhysRevLett.91.025503.

Koslowski, M., CuitiÃo, A.M., Ortiz, M., 2002. A phase-field theory of dislocation dynamics, strain hardening and hysteresis in ductile single crystals. J. Mech. Phys. Solids 50 (12), 2597–2635. doi:10.1016/S0022-5096(02)00037-6.

Kresse, G., Furthmüller, J., 1996. Efficient iterative schemes for *ab initio* total-energy calculations using a plane-wave basis set. Phys. Rev. B 54 (16), 11169–11186. doi:10.1103/PhysRevB.54.11169.

Kresse, G., Joubert, D., 1999. From ultrasoft pseudopotentials to the projector augmented-wave method. Phys. Rev. B 59 (3), 1758–1775. doi:10.1103/PhysRevB.59.1758.

Kumar, A., Kedjar, B., Su, Y., Thilly, L., Beyerlein, I.J., 2020. Atomic-level calculations and experimental study of dislocations in InSb. J. Appl. Phys. 127 (13), 135104. doi:10.1063/1.5139285.

Li, X.Y., Yang, W., 2006. Atomistic simulations for the evolution of a U-shaped dislocation in fcc Al. Phys. Rev. B 74 (14), 144108. doi:10.1103/PhysRevB.74.144108.

Marinica, M.-C., Ventelon, L., Gilbert, M.R., Proville, L., Dudarev, S.L., Marian, J., Bencteux, G., Willaime, F., 2013. Interatomic potentials for modelling radiation defects and dislocations in tungsten. J. Phys.: Condens. Matter 25 (39), 395502. doi:10.1088/0953-8984/25/39/395502.

Martínez, E., Marian, J., Arsenlis, A., Victoria, M., Perlado, J.M., 2008. Atomistically informed dislocation dynamics in fcc crystals. J. Mech. Phys. Solids 56 (3), 869–895. doi:10.1016/j.jmps.2007.06.014.

Methfessel, M., Paxton, A.T., 1989. High-precision sampling for Brillouin-zone integration in metals. Phys. Rev. B 40 (6), 3616–3621. doi:10.1103/PhysRevB.40.3616.

Monkhorst, H.J., Pack, J.D., 1976. Special points for Brillouin-zone integrations. Phys. Rev. B 13 (12), 5188–5192. doi:10.1103/PhysRevB.13.5188.

Monnet, G., Terentyev, D., 2009. Structure and mobility of the $\frac{1}{2}\langle 111\rangle\{112\}$ edge dislocation in bcc iron studied by molecular dynamics. Acta Mater. 57 (5), 1416–1426. doi:10.1016/j.actamat.2008.11.030.
Peng, X., Mathew, N., Beyerlein, I.J., Dayal, K., Hunter, A., 2020. A 3d phase field dislocation dynamics model for body-centered cubic crystals. Comput. Mater. Sci. 171, 109217. doi:10.1016/j.commatsci.2019.109217.
Perdew, J.P., Burke, K., Ernzerhof, M., 1996. Generalized gradient approximation made simple. Phys. Rev. Lett. 77 (18), 3865–3868. doi:10.1103/PhysRevLett.77.3865.
Po, G., Cui, Y., Rivera, D., Cereceda, D., Swinburne, T.D., Marian, J., Ghoniem, N., 2016. A phenomenological dislocation mobility law for bcc metals. Acta Mater. 119, 123–135. doi:10.1016/j.actamat.2016.08.016.
Qian, J., Wu, C.Y., Fan, J.L., Gong, H.R., 2018. Effect of alloying elements on stacking fault energy and ductility of tungsten. J. Alloys Compd. 737, 372–376. doi:10.1016/j.jallcom.2017.12.042.
Qiu, D., Zhao, P., Shen, C., Lu, W., Zhang, D., Mrovec, M., Wang, Y., 2019. Predicting grain boundary structure and energy in BCC metals by integrated atomistic and phase-field modeling. Acta Mater. 164, 799–809. doi:10.1016/j.actamat.2018.11.023.
Raabe, D., 1995. Contribution of $\{123\}<111>$ slip systems to deformation of b.c.c. metals. Phys. Stat. Solidi (a) 149 (2), 575–581. doi:10.1002/pssa.2211490208.
Reuss, A., 1929. Berechnung der Fließgrenze von Mischkristallen auf Grund der Plastizitätsbedingung für Einkristalle. Z. Angew, Math. Mech. 9 (1), 49–58. doi:10.1002/zamm.19290090104.
Rodney, D., Finel, A., 2001. Phase field methods and dislocationss. MRS Online Proceedings Library Archive 652, Y4.9. doi:10.1557/PROC-652-Y4.9.
Rodney, D., Le Bouar, Y., Finel, A., 2003. Phase field methods and dislocations. Acta Mater. 51 (1), 17–30. doi:10.1016/S1359-6454(01)00379-2.
Romaner, L., Ambrosch-Draxl, C., Pippan, R., 2010. Effect of rhenium on the dislocation core structure in tungsten. Phys. Rev. Lett. 104 (19), 195503. doi:10.1103/PhysRevLett.104.195503.
Ruffini, A., Le Bouar, Y., Finel, A., 2017. Three-dimensional phase-field model of dislocations for a heterogeneous face-centered cubic crystal. J. Mech. Phys. Solids 105, 95–115. doi:10.1016/j.jmps.2017.04.008.
Shen, C., Wang, Y., 2003. Phase field model of dislocation networks. Acta Mater. 51 (9), 2595–2610. doi:10.1016/S1359-6454(03)00058-2.
Shen, C., Wang, Y., 2004. Incorporation of γ-surface to phase field model of dislocations: simulating dislocation dissociation in fcc crystals. Acta Mater. 52, 683–691.
Shimokawa, T., Kitada, S., 2014. Dislocation multiplication from the Frank-Read source in atomic models. Mater. Trans. 55 (1), 58–63. doi:10.2320/matertrans.MA201319.
Shishvan, S.S., Mohammadi, S., Rahimian, M., 2008. A dislocation-dynamics-based derivation of the Frank-Read source characteristics for discrete dislocation plasticity. Modelling Simul. Mater. Sci. Eng. 16 (7), 075002. doi:10.1088/0965-0393/16/7/075002.
Stricker, M., Sudmanns, M., Schulz, K., Hochrainer, T., Weygand, D., 2018. Dislocation multiplication in stage II deformation of fcc multi-slip single crystals. J. Mech. Phys. Solids 119, 319–333. doi:10.1016/j.jmps.2018.07.003.
Su, Y., Ardeljan, M., Knezevic, M., Jain, M., Pathak, S., Beyerlein, I.J., 2020. Elastic constants of pure body-centered cubic Mg in nanolaminates. Comput. Mater. Sci. 174, 109501. doi:10.1016/j.commatsci.2019.109501.
Su, Y., Xu, S., Beyerlein, I.J., 2019. Density functional theory calculations of generalized stacking fault energy surfaces for eight face-centered cubic transition metals. J. Appl. Phys. 126 (10), 105112. doi:10.1063/1.5115282.
Su, Y., Xu, S., Beyerlein, I.J., 2019. *Ab initio*-informed phase-field modeling of dislocation core structures in equal-molar CoNiRu multi-principal element alloys. Modelling Simul. Mater. Sci. Eng. 27 (8), 084001. doi:10.1088/1361-651X/ab3b62.
Terentyev, D., Bakaev, A., Neck, D.V., Zhurkin, E.E., 2016. Glide of dislocations in $<111>\{321\}$ slip system: an atomistic study. Philos. Mag. 96 (1), 71–83. doi:10.1080/14786435.2015.1126369.
Terentyev, D., Bonny, G., Domain, C., Pasianot, R.C., 2010. Interaction of a $\frac{1}{2}\langle 111\rangle$ screw dislocation with Cr precipitates in bcc Fe studied by molecular dynamics. Phys. Rev. B 81 (21), 214106. doi:10.1103/PhysRevB.81.214106.
Voigt, W., 1889. Ueber die Beziehung zwischen den beiden Elasticitätsconstanten isotroper Körper. Ann. Phys. 274 (12), 573–587. doi:10.1002/andp.18892741206.
Wang, Y.U., Jin, Y.M., Cuitiño, A.M., Khachaturyan, A.G., 2001. Nanoscale phase field microelasticity theory of dislocations: model and 3d simulations. Acta Mater. 49 (10), 1847–1857. doi:10.1016/S1359-6454(01)00075-1.
Warlimont, H., Martienssen, W. (Eds.), 2018. Springer Handbook of Materials Data, 2nd edition. Springer International Publishing.
Weinberger, C.R., Boyce, B.L., Battaile, C.C., 2013. Slip planes in bcc transition metals. Int. Mater. Rev. 58 (5), 296–314. doi:10.1179/1743280412Y.0000000015.
Xiang, Y., Cheng, L.-T., Srolovitz, D.J., E, W., 2003. A level set method for dislocation dynamics. Acta Mater. 51 (18), 5499–5518. doi:10.1016/S1359-6454(03)00415-4.
Xu, S., Che, R., Xiong, L., Chen, Y., McDowell, D.L., 2015. A quasistatic implementation of the concurrent atomistic-continuum method for FCC crystals. Int. J. Plast. 72, 91–126. doi:10.1016/j.ijplas.2015.05.007.
Xu, S., Chen, X., 2019. Modeling dislocations and heat conduction in crystalline materials: atomistic/continuum coupling approaches. Int. Mater. Rev. 64 (7), 407–438. doi:10.1080/09506608.2018.1486358.
Xu, S., Mianroodi, J.R., Hunter, A., Beyerlein, I.J., Svendsen, B., 2019. Phase-field-based calculations of the disregistry fields of static extended dislocations in FCC metals. Philos. Mag. 99 (11), 1400–1428. doi:10.1080/14786435.2019.1582850.
Xu, S., Mianroodi, J.R., Hunter, A., Svendsen, B., Beyerlein, I.J., 2020. Comparative modeling of the disregistry and Peierls stress for dissociated edge and screw dislocations in Al. Int. J. Plast. 129, 102689. doi:10.1016/j.ijplas.2020.102689.
Xu, S., Payne, T.G., Chen, H., Liu, Y., Xiong, L., Chen, Y., McDowell, D.L., 2018. PyCAC: The concurrent atomistic-continuum simulation environment. J. Mater. Res. 33 (7), 857–871. doi:10.1557/jmr.2018.8.
Xu, S., Rigelesaiyin, J., Xiong, L., Chen, Y., McDowell, D.L., 2018. Generalized continua concepts in coarse-graining atomistic simulations. In: Generalized Models and Non-classical Approaches in Complex Materials 2. Springer, Cham, pp. 237–260. doi:10.1007/978-3-319-77504-3_12.
Xu, S., Smith, L., Mianroodi, J.R., Hunter, A., Svendsen, B., Beyerlein, I.J., 2019. A comparison of different continuum approaches in modeling mixed-type dislocations in Al. Modelling Simul. Mater. Sci. Eng. 27 (7), 074004. doi:10.1088/1361-651X/ab2d16.
Xu, S., Startt, J.K., Payne, T.G., Deo, C.S., McDowell, D.L., 2017. Size-dependent plastic deformation of twinned nanopillars in body-centered cubic tungsten. J. Appl. Phys. 121 (17), 175101. doi:10.1063/1.4982754.
Xu, S., Su, Y., 2018. Dislocation nucleation from symmetric tilt grain boundaries in body-centered cubic vanadium. Phys. Lett. A 382 (17), 1185–1189. doi:10.1016/j.physleta.2018.03.002.
Xu, S., Su, Y., Beyerlein, I.J., 2019. Modeling dislocations with arbitrary character angle in face-centered cubic transition metals using the phase-field dislocation dynamics method with full anisotropic elasticity. Mech. Mater. 139, 103200. doi:10.1016/j.mechmat.2019.103200.
Xu, S., Su, Y., Chavoshi, S.Z., 2018. Deformation of periodic nanovoid structures in Mg single crystals. Mater. Res. Express 5 (1), 016523. doi:10.1088/2053-1591/aaa678.
Xu, S., Su, Y., Smith, L., Beyerlein, I.J., 2020. Generalized stacking fault energy curves for six body-centered cubic refractory metals. Materials Cloud Archive https://archive.materialscloud.org/2020.0001/.
Xu, S., Xiong, L., Chen, Y., McDowell, D.L., 2016. An analysis of key characteristics of the Frank-Read source process in FCC metals. J. Mech. Phys. Solids 96, 460–476. doi:10.1016/j.jmps.2016.08.002.
Xu, S., Xiong, L., Chen, Y., McDowell, D.L., 2017. Comparing EAM potentials to model slip transfer of sequential mixed character dislocations across two symmetric tilt grain boundaries in Ni. JOM 69 (5), 814–821. doi:10.1007/s11837-017-2302-1.
Xu, S., Xiong, L., Chen, Y., McDowell, D.L., 2017. Shear stress- and line length-dependent screw dislocation cross-slip in FCC ni. Acta Mater. 122, 412–419. doi:10.1016/j.actamat.2016.10.005.

Yan, J.-A., Wang, C.-Y., Wang, S.-Y., 2004. Generalized-stacking-fault energy and dislocation properties in bcc Fe: A first-principles study. Phys. Rev. B 70 (17), 174105. doi:10.1103/PhysRevB.70.174105.

Yang, C., Qi, L., 2019. Modified embedded-atom method potential of niobium for studies on mechanical properties. Comput. Mater. Sci. 161, 351–363. doi:10.1016/j.commatsci.2019.01.047.

Yang, L.H., Söderlind, P., Moriarty, J.A., 2001. Accurate atomistic simulation of $(a/2) < 111 >$ screw dislocations and other defects in bcc tantalum. Philos. Mag. A 81 (5), 1355–1385. doi:10.1080/01418610108214446.

Zbib, H.M., Rhee, M., Hirth, J.P., 1998. On plastic deformation and the dynamics of 3d dislocations. Int. J. Mech. Sci. 40 (2–3), 113–127. doi:10.1016/S0020-7403(97)00043-X.

Zhang, R.F., Wang, J., Beyerlein, I.J., Germann, T.C., 2011. Twinning in bcc metals under shock loading: a challenge to empirical potentials. Philos. Mag. Lett. 91 (12), 731–740. doi:10.1080/09500839.2011.615348.

Zhang, S.H., Zhang, R.F., 2017. AELAS: Automatic ELAStic property derivations via high-throughput first-principles computation. Comput. Phys. Comm. 220, 403–416. doi:10.1016/j.cpc.2017.07.020.

Zhang, X., Tang, J., Deng, L., Zhong, G., Liu, X., Li, Y., Deng, H., Hu, W., 2017. The effects of interstitial impurities on the mechanical properties of vanadium alloys: A first-principles study. J. Alloys Compd. 701, 975–980. doi:10.1016/j.jallcom.2017.01.135.